Experimental Constraints on Parameters Controlling the Difference in the Eruptive Dynamic of Phonolitic Magmas: the case from Tenerife (Canary Islands)

Joan Andújar, Bruno Scaillet

Experimental Constraints on Parameters Controlling the Difference in the Eruptive Dynamic of Phonolitic Magmas: the case from Tenerife (Canary Islands)

JOAN ANDÚJAR[*,a] AND BRUNO SCAILLET[a]

a. CNRS-INSU/UNIVERSITÉ D'ORLÉANS/BRGM, INSTITUT DES SCIENCES DE LA TERRE (ISTO), UMR 6113, 1A, RUE DE LA FÉROLLERIE-45071 ORLÉANS CEDEX 2 (FRANCE)

* **Corresponding author :** Joan Andújar

phone number : (+33) 2 38 25 53 87
Fax: (+33) 02 38 63 64 88
e-mail address: Juan.Andujar@cnrs-orleans.fr

Bruno Scaillet e-mail address: bscaille@cnrs-orleans.fr

KEY WORDS: *Phase equilibria, phonolite, experimental petrology, eruptive dynamic, flank eruption, Tenerife*

ABSTRACT

We have performed phase equilibrium experiments to determine the pre-eruptive conditions of the explosive eruption of Montaña Blanca (2020 BP) that occurred from a satellite vent located in the east flank of Teide volcano (Tenerife Island). Crystallization experiments were performed using a phonolitic obsidian from the fall out deposit that contains 5 wt% anorthoclase, diopside and magnetite with minor amounts of biotite and ilmenite, set in a glassy matrix that contains microlites of Ca-rich alkali feldspars. Temperature was varied between 850ºC and 800ºC, and pressure between 200MPa to 50 MPa. The oxygen fugacity (fO_2) was varied between NNO+0.2 (0.2 log units above to the Ni-NiO solid buffer) to NNO-2, whilst dissolved water contents varied from 7 to 1.5 wt%. Comparison between natural and experimental phase proportions and compositions indicates that the main body of phonolite magma was stored at 850±15ºC, 50±20MPa, 2.5±0.5wt% H_2O at an fO_2 around NNO-0.5 prior to eruption, equivalent to depths between 1 to 2 km below the surface. Some clinopyroxene hosting H_2O-rich melt inclusions possibly originates from intermittent supply of phonolitic magma stored at somewhat deeper levels (100 MPa). The Ca and Fe-rich composition of alkali feldspar phenocrysts rims and microlites attests to the intrusion of a mafic magma in the reservoir just prior to eruption, as borne out by banded pumices appearing in the later products of the eruptive sequence. The comparison with other phonolitic magmas from Tenerife and elsewhere (e.g., Vesuvius, Laacher See) shows that differences in the eruptive dynamic of phonolitic magmas can be correlated to differences in storage depths, along with variation in pre-eruptive volatile contents.

INTRODUCTION

A potential eruption in densely populated regions represents a serious threat to human being and associated infrastructures, and it is crucial to develop hazard assessment campaigns for minimizing the risk of future volcanic events. This task is undertaken by considering the eruptive history of the volcano, which very often records significant variations in eruptive styles. Regardless of the extruded volume of material, the eruptive activity can be divided in three different major categories: purely effusive; transient explosive and sustained explosive activity (which generates plinian deposits). As these three eruptive regimes generate different hazards, there is a crucial need to understand the factors responsible for either type of eruption. The proposed causes for explaining the difference in the eruptive dynamic involve differences in volatile content

of the magmas, vent conditions, processes occurring during magma ascent to the surface (e.g. magma degassing in the conduit, differences in ascent velocity; variation of the rheological properties of the magma; Sparks et al., 1994; Martel et al., 1998; Martel & Schmidt, 2003; Castro & Mercer, 2004). However, each volcano is specific in terms of eruptive behaviour, magma composition, and thermodynamic conditions which makes it necessary to investigate them on a case-by-case basis.

Tenerife Island is a case in point. It hosts the active Teide-Pico Viejo volcano, which has slowly evolved from a primitive to highly differentiated edifice, becoming one of the potentially most hazardous volcanoes in the Canary Islands. The most recent eruptive activity of this stratovolcano has ejected basalts to phonolites (Carracedo et al., 2007; Ablay et al., 1998). Phonolitic activity is mainly focused at Teide volcano which has chiefly developed an effusive or transient explosive activity over the last 35 kyrs (Carracedo et al., 2007; Martí et al., 2008), with only two sustained explosive eruptions derived from one of the numerous radially located flank vents (Ablay et al., 1995; Ablay & Martí, 2000; Carracedo & Rodríguez-Badiola, 2006; Martí et al., 2008). Thus, it is crucial to determine what factors control the eruptive dynamic in a volcanic system like Teide, which is characterised by erupting magmas with a similar composition yet displaying a broad range of eruptive styles over the last 35 kyrs (Carracedo et al., 2007; Ablay et al., 1998). Within this context, we have performed phase equilibrium experiments on the plinian products of the 2 ka Montaña Blanca eruption, the most explosive and one of the most recent phonolite eruption, of this volcanic complex. The combination of the results obtained from this and previous works on Teide, as well as on other phonolitic volcanoes, allows us to clarify the role that pre-eruptive storage conditions have on eruptive behaviour of phonolitic magmas, in particular pressure.

GEOLOGICAL SETTING

The volcanic activity of Tenerife started at >10Ma until present and generated three main volcanic complexes. The first complex involved the construction of the mafic alkaline shield which forms the 90% of the entire volume of the island, being however almost all submerged, apart from the peripheral edifices of Teno, Anaga and Roque del Conde (Ancochea et al., 1990; Martí et al., 1994; Ablay & Martí, 2000). The second is the Central complex, whose construction occurred between 4 and 0.2 Ma, and which is subdivided into a Lower Group, dominated by mafic to intermediate compositions, and an Upper Group formed by the products of three felsic volcanic

cycles characterised by abundant explosive eruptions that culminated with three caldera-forming eruptions (Martí et al. 1994, 1997; Martí & Gudmunsson, 2000). The third is the currently active Teide-Pico Viejo stratovolcano (0.19 Ma to present), the focus of the present study, and the basaltic rifts.

The Teide-Pico Viejo volcanic complex (T-PV) is located inside the depression of the Las Cañadas caldera of the second complex and consists of two twin stratovolcanoes and numerous satellite vents that have generated lava outflows that partially infilled the Las Cañadas depression and in some cases overflowed to adjacent valleys (Hausen, 1956; Araña, 1971; Ablay et al., 1998; Ablay & Martí, 2000; Carracedo et al., 2007). The first stage of the Teide-Pico Viejo complex was dominated by the eruption of mafic to intermediate products whereas phonolitic volcanism started about 35 ka ago (Carracedo et al., 2007; Ablay et al., 1998; Ablay & Martí, 2000; Martí et al,. 2008). Although most eruptions that occurred in the last 35 ka in the T-PV volcanic complex are basaltic in composition, phonolitic magmas are volumetrically more abundant (Martí et al., 2008). The eruptive style of these phonolitic events has been dominated by effusive to transient explosive eruptions that generated lava flows and ash columns of only several km high. These events produced scoria and spatter deposits, together with thick lava flows (Ablay & Martí 2000; Martí et al., 2008). In addition to these "quiet" felsic eruptions, two plinian events from flank vents of the Pico Teide stratovolcano occurred in recent times. One of them occurred at the North side of Teide although the location of the vent that generated the associated deposits has not been identified yet (Martí et al. 2008). The second corresponds to the well characterised 2020 BP sub-plinian eruption of Montaña Blanca (MB), the target of the present study, which is now briefly described in the following section.

Montaña Blanca

Montaña Blanca is the only well known substantial post-caldera explosive eruption which occurred from a satellite vent located in the East flank of Teide (Fig.1). It has a total volume of 0.05 Km^3 DRE (Martí et al., 2008) and forms one of the most remarkable topographic features occurring in the flank of the volcano. This eruption has been the focus of several stratigraphic/petrological studies which provide different interpretations for this event. Carracedo et al. (2007) and Carracedo & Rodríguez-Badiola (2006), using statrigraphic arguments, distinguished eight different phases for this event. In contrast, Ablay et al. (1995), based on detailed field, petrological

/geochemical studies of the different phases of this eruption, distinguished only three different units for this eruption. In our study we have adopted the framework of Ablay et al. (1995) as a guide for our experimental work, because these authors provide detailed information on erupted volumes, field relationships, petrological and geochemical data of the eruptive units, as well as thermo-barometric and volatile content determinations which allowed them to propose a model for the magmatic reservoir of Montaña Blanca prior to the eruption. The main findings of Ablay et al. (1995) concerning the products of the three different units of the Montaña Blanca eruption are shown in Fig. (1) and Table A1 and briefly summarised here below.

The multi-episode eruption of Montaña Blanca started from a vent located in Las Cañadas Caldera floor (2200m a.s.l.; Carracedo et al., 2007; Ablay et al., 1995) which emitted blocky tephriphonolite lavas that produced the first and oldest unit, termed the Arenas Blancas member. According to Ablay et al. (1995), the Arenas Blancas products are geochemically related to those from central Teide vent, suggesting that the initial phase of the MB eruption acted as a satellite vent of pico Teide. The second unit, known as Lower Montaña Blanca member (LMB), comprises phonolitic products of three different vents which are aligned along a fissure located southward of the complex. After the eruption of the LMB, the eruptive activity stopped long enough for the production of a paleosol. The paleosol separates the LMB from the Upper Montaña Blanca member (UMB) which is the volumetrically dominant member of Montaña Blanca eruptions. The stratigraphical, geochemical, petrological data and Fe-Ti oxide geothermometry allowed the reconstruction of the magma reservoir structure before eruption of the UMB unit (Fig.1b, Table A1), as well as the temporal evolution of this volcanic event. Ablay et al. (1995) proposed a shallow (3-4 km) compositionally and thermally zoned reservoir where three different magmas with a different degree of evolution, coexisted before the eruption (Fig.1b). The coldest phonolitic magma of unit UMBIII was located atop the reservoir, underlained by the unit UMBII, which forms the main volume of the reservoir, and by Unit UMBI magma from which the two first units were evolving. A more mafic magma (phonotephrite) is thought to underlain the Unit I magma (Fig. 1b).

The UMB eruption erupted via a lateral propagating dyke that initially tapped UMBI magma, located in the middle part of the reservoir. Unit I corresponds to the products of an initial effusive phase which ejected the less evolved phonolite of the UMB known as El Tabonal Negro. The lack of paleosols development on Unit I

indicates a short time interval (several months) separating this eruption from the next volcanic event, unit UMBII (Ablay et al., 1995). This second eruption occurred from vents located atop of the pre-existing Montaña Blanca edifice, which at the time of the eruption could have reached heights of about 300-400 m above the caldera floor (about 2500-2600 m a.s.l., Carracedo et al. 2007, Ablay et al. 1995), and ejected a highly evolved phonolite during a plinian phase that generated a 10 km high eruptive column, with an extensive fall out deposit emplaced to the NE of the vent (Ablay et al., 1995, 1998; Martí et al., 2008). The fall out deposit consists mainly of phonolitic pumice and minor amounts (< 3 wt%) of black phonolitic pyroclastic obsidians. According to these authors, this second eruption tapped the UMBII magma essentially from the bottom upwards. UMBII ended with the eruption of compositionally banded pumices characterised by a dominant phonolitic member identical to the phonolitic pumice composition, and a subordinate phonolitic-tephritic component. The eruption waned to fire-fountaining and effusive domes at its later stages, erupting the most evolved component products termed Unit III (Fig.1b).

The phonolitic products of UMB units are petrologically and chemically broadly similar (Table A1). Rocks have very low crystal content (1-4 vol%), with mainly alkali feldspar, biotite, clinopyroxene, magnetite ± ilmenite, apatite, and the differences in bulk rock compositions between the units are < 1 wt% for most oxides (Ablay et al. 1995; 1998). However, the trace element contents of the UMB magmas reveal significant different degree of evolution (Ablay et al., 1995; 1998). In particular, the Zr content of the phonolitic magmas from Tenerife and those erupted during the UMB member can be used as an indicator of fractionation, with more evolved compositions having higher Zr contents. Thus, within the UMB magmas, the UMBIII is the most evolved composition with the highest Zr and Ce contents (1142 ppm and 214 ppm, respectively). In contrast, the UMBI magma appears to be the least evolved phonolite emitted during this eruption, with 988 ppm Zr and 205 ppm Ce. The UMBII phonolite trace composition falls in between these two sub-units (1114 ppm Zr, 210 ppm Ce; Table A1, Fig.1b).

Pre-eruptive temperatures were determined by Ablay et al (1995; 1998) using co-existing Fe-Ti oxides and the model of Sack & Ghiorso (1991) and confirm the above Zr-trend. Results yield a temperature of 877±22ºC for UMB I, 825-860ºC for the pumice and obsidian lithics of UMB II, and 775ºC for rocks of UMB III. The fO_2 was constrained to be between NNO-0.5 to FMQ. Temperatures as low as 755ºC were

obtained for some pumices of Unit II, though it is not sure that the magnetite and ilmenite pairs used in the calculations are in equilibrium (Ablay et al., 1995).

Melt inclusions in clinopyroxene from fall-out pumices suggest water contents between 3 to 4.5 wt% H_2O dissolved in the melt, with an extreme value of 6.5 wt% (Ablay et al., 1995). The melt inclusions has also significant amounts of dissolved Cl and F (~3000 ppm each). Using these volatile contents and the water solubility model of Carroll & Blank (1997) calibrated for Teide sodic phonolites, Ablay et al. (1995) inferred a storage pressure of 100 MPa.

Andújar et al. (2010) provided constraints on storage conditions from the last phonolitic eruption of Teide (so-called Lavas Negras; 1150 yr BP, Carracedo et al. 2007) by performing phase equilibrium experiments. They reported pre-eruptive conditions of 900ºC, 150 MPa and water contents of 3 wt%, which are comparable to those previously inferred for Montaña Blanca. Thus, we have used this information as a guide for our experimental work.

Starting Material

In order to constrain the pre-eruptive conditions of the Montaña Blanca magma, we have performed phase equilibrium experiments following procedures similar to those used for establishing the pre-eruptive conditions of Pinatubo or Mt Pelée or Vesuvius recent eruptions (Scaillet & Evans, 1999; Martel et al., 1998; Scaillet et al., 2008). We have used as starting material for our experiments a piece of fresh glassy pyroclastic obsidian collected from the fall out pumice deposit of UMB II (Ablay et al., 1995).

Despite that pumices are the volumetrically dominant material in this unit, we have chosen to use the pyroclastic obsidian occurring within the fall-out deposit as starting material for the following reasons: a) pumices tend to have a weathered outer rim whereas obsidians are characterised by their relative freshness, b) the mineral assemblage and mineral composition of the obsidian is identical to that of the pumices (see Ablay et al., 1995), c) differences between bulk composition of the obsidian and the pumice are within analytical errors (<0.5 wt% for Al_2O_3 and Na_2O; Table A1), d) the trace element contents of the pyroclastic obsidian (Zr, Ba, Ce, Cl and Sr; Table A1) match those of pumices; e) Fe-Ti oxides are in equilibrium and allows calculations of pre-eruptive T and fO_2 as reported by Ablay et al. (1995, 1998).

The geochemical and petrological similarities between the pyroclastic obsidian and the UMBII pumices indicate: 1) that the composition of the obsidian was not affected by any syn-eruptive processes that might have occurred in the conduit during magma uprise; 2) that the mineral assemblage and composition that we have determined for the obsidian correspond to those acquired at the storage levels rather than at syn-eruptive conditions, because the high decompression rates which are associated to plinian eruptions prevent the crystallization of new phenocrysts, rim-overgrowths and microlites (i.e., Martel et al., 2006, Castro & Gardner, 2008; Martel & Schmidt, 2003). We therefore consider that our starting product (pyroclastic obsidian) is compositionally representative of the UMBII phonolitic magma that generated the sub-plinian deposit of the MB eruption, both being juvenile products emitted during the same eruptive phase. Accordingly, the phase equilibria established on the pyroclastic obsidian are useful for understanding the conditions that led to the plinian eruption of UMBII.

Several thin sections of the obsidian were prepared and studied under the petrographic microscope and with the scanning electron microscope (SEM) with the aim of identifying the mineralogy of the sample (Figs.2a and 2b). Phase proportions were obtained by mass-balance calculations using the composition of natural minerals and glass. The sample contains ~5 wt.% of mainly euhedral anorthoclase (4 wt.%; Or_{33-36} An_{4-1} Ab_{61-64}, with 0.1-0.4 wt% FeO*), diopside (0.7 wt%, Mg#=68 ($Mg\#=100[Mg/(Mg+Fe^*))]$); $En_{36}Fs_{16}Wo_{45}$), and magnetite (0.5 wt%, Mg#=4). Biotite (Mg#=58) and ilmenite are present in trace amounts, the total of such phases being < 0.1 wt.% (Figs.2a and 2b, Table 1). The phenocrysts are set in a non-vesiculated glassy matrix containing Na-Ca-rich anorthoclase microlites (Or_{12-16} An_{10-12} Ab_{72-77}, with 0.9-1.6 wt% FeO*; Fig.2b, Table 1). The glassy matrix is phonolitic (59.8 wt% SiO_2, 10 wt% Na_2O, 6.0 wt% K_2O) with totals of ~97.5 wt% suggesting water contents of 2.5 wt% calculated by the difference method (Table 1).

The An content variation of alkali feldspar phenocrysts is relatively small when compared to those documented in feldspars from calc-alkaline magmas (i.e., variations of about 15-20 mol%). However, although subtle, two different categories can be distinguished: one population with An contents of ~1-2 mole% (fspbig, Fig. 3a) and one with An contents varying between 2.5 to 4 mole % (fsppt, Fig. 3, Table 1). In the latter, the crystals are characterised by various zonation patterns. Some crystals are normally zoned from An_4 to An_3, whilst other present core compositions of An_{4-3} and rims of

An$_{2.5-1}$. Some crystals display cyclic zonations of small amplitude all over their length (i.e., fspbig in Fig.3b). A remarkable feature is that all anorthoclase phenocrysts are characterised by an anorthitic-rich (and orthoclase-poor), and Fe-rich rim that resembles the composition of the microlites of the glassy matrix (An$_{10-11}$, 0.9-1.2 wt% FeO*; Table 1).

In contrast, clinopyroxene phenocrysts are compositionally homogeneous without significant core to rim zonation (Fig.4). The trace minerals do not display any significant compositional zoning.

EXPERIMENTAL AND ANALYTICAL TECHNIQUES

Preparation of the starting material

The obsidian was first finely ground in an agate mortar and melted twice, with grinding in between, in a Pt crucible at 1400ºC during 5 hours in open atmosphere. Electron Microprobe Analyses (EMPA) of the starting glass show it to be homogeneous with no significant Na or Fe loss compared to the starting rock (Table 1). The resulting dry glass was then ground to obtain the powder that was used as starting material for the phase equilibrium experiments and stored in an oven at 120ºC.

Experimental equipment and strategy

A total of 48 experiments were performed at the ISTO experimental laboratory, using the same experimental apparatus and procedure followed by Scaillet et al. (1992), Costa et al. (2004), Di Carlo et al. (2006), as briefly summarized below. Experiments were carried out in an Internally Heated Pressure Vessel (IHPV) operating vertically, loaded with different Ar-H$_2$ mixtures at room temperature to achieve the desired fO$_2$ conditions. Experimental fH$_2$ was recorded by using Ni-Pd-O sensors run at the same conditions as experimental capsules (see below). Total pressure was recorded by a transducer calibrated against a Heise Bourdon gauge with an uncertainty of ±20 bars. Double-winding molybdenum and kanthal furnaces were used which allow near-isothermal conditions (gradient <2-3ºC/cm) along a 3 cm long hot spot. Temperature was measured using three S- or K-type thermocouples with an accuracy of ±5ºC. A rapid-quench technique was systematically used which allows isobaric cooling rates of >100ºC/s (e.g., Martel et al., 1999; Di Carlo et al., 2006). In all runs reported here, the

drop quench was successful as indicated by the rise in total pressure upon the falling of the sample holder into the cold (bottom) part of the vessel.

Based on available P-T-H_2O pre-eruptive constraints summarised above, experiments were mainly conducted at 850ºC, pressures of 200, 150, 100 and 50 MPa and at fO_2 ~NNO. We have also conducted experiments at 800ºC, 200 and 100 MPa at NNO with the aim of studying the effect of temperature on phase relations and composition. Three runs were also perfomed at FMQ at 850ºC so as to study the effect of oxygen fugacity on phase equilibria at this temperature (Table 2).

Capsule preparation

We used Au capsules (1.5 cm long, 2.5 mm inner diameter, 0.2 mm wall thickness) which minimizes the Fe-loss under reducing conditions. Distilled H_2O was first loaded, then silver oxalate as the source of CO_2 for H_2O-undersaturated runs, and then the glass powder. Capsules were weighed and then welded using an electric-graphite welder. After welding, capsules were re-weighed and if no significant weight loss occurred (considered to occur when a difference > 0.0004 g in weight was noted), they were left in an oven for a few hours at 100ºC, to ensure homogeneous H_2O distribution. Both the amount of H_2O+CO_2 and fluid/silicate ratio were maintained constant (3 ± 0.5 mg of H_2O+CO_2, and 30 mg silicate). At a given T-P conditions, various starting H_2O-CO_2 mixtures were explored: XH_2O_{in} being defined as $H_2O/(H_2O+CO_2)$ (in moles), it was varied in the range 1-0.47 (Table 2).

Typically, a total of six experimental charges plus one containing a Ni-Pd-O redox sensor to monitor the prevailing fH_2 were loaded into the furnace and ran at the desired T-P-fO_2 (Table 2). The Ni-Pd-O sensor was prepared following the procedure of Taylor et al. (1992). After the experiment, the analysis of the metallic phase allowed us to calculate the fH_2/fO_2 of the system (Pownceby & O'Neill, 1994; see below).

Run durations varied between 7 and 18 days depending on pressure. Runs were terminated by first using the drop quench device and then switching off the power supply. After the experiment, capsules were checked for leaks, opened, and half of the run product was embedded in a probe mount with an epoxy resin and polished for optical observation, and subsequent EMPA and SEM analyses.

Water content, fH_2, fO_2 in the capsules

The variation of the XH_2O_{in} in the capsules, achieved by using different mixtures of H_2O+CO_2, allowed us to explore different water fugacities, and thus melt H_2O content, in the experiments (Table 2). The amount of dissolved water in the glass of H_2O-saturated and reduced charges was determined by performing FTIR analyses. As the composition of the natural obsidian is equal to the composition used by Carroll & Blank (1997) we have used the same analytical conditions and parameters (e.g., extinction coefficients $\in 5200$ $\in 4500$) than those authors (Table 3). As the water solubility of our iron-poor melts is not expected to vary significantly with oxygen fugacity (e.g., Moretti & Papale, 2004; Papale et al., 2006; Berndt et al. 2005) we have extrapolated the amounts found by FTIR at reduced conditions to experiments conducted at higher fO_2. Then, the water content of the charges with $XH_2O_{in}<1$, ran at the same temperature and pressure than the saturated charge, was calculated by multiplying the water content determined by FTIR at saturated conditions by the initial mole fraction of water loaded in the capsule (XH_2O_{in}, Table 2), which is equivalent to assume ideal behaviour of the H_2O-CO_2 fluid binary (e.g., Berndt et al., 2005). For experiments where the water content of the H_2O-saturated charge could not be determined by FTIR, (e.g., experiments conducted at 800ºC which are too crystal-rich), the melt water content of the saturated charge was computed using the solubility model of Carroll & Blank (1997). As water solubility depends on melt composition (e.g., Carroll & Blank 1997, Schmidt & Behrens 2008) the use of this model will minimize such effect in our water determinations, because these authors used the same pyroclastic obsidian as starting material. The amount of CO_2 dissolved in a phonolitic melt in the range of pressures explored by this work can be calculated to be < 0.1 wt% (Morizet et al., 2002). The presence of such a small amount of CO_2 dissolved in the phonolitic melt at the explored range of pressure and temperature will have a negligible effect on the solubility of water. We note that the various procedures used in our work for determining the water content of quenched glasses (FTIR, Carroll & Blank (1997) solubility model, summation deficit) yielded results that agree to within < 0.5 wt% H_2O.

As previously mentioned, Ni-Pd-O sensors were used with the aim of determining the prevailing fH_2 and, ultimately, the fO_2 of the experiments (see below). However, in some experiments the metallic sensors failed and the prevailing fH_2 could not be determined directly. The fH_2 of those runs was determined by using an empirical calibration curve between the H_2 pressure added to the autoclave at room temperature and the the fH_2 of the successful sensors (Table 2).

Once the intrinsic $f\mathrm{H}_2$ is known, the $f\mathrm{O}_2$ can be determined by using the dissociation constant of water (Robie et al., 1979) and knowing the $f\mathrm{H}_2\mathrm{O}$ at the experimental temperature and pressure. The $f\mathrm{H}_2\mathrm{O}$ was calculated as $f\mathrm{H}_2\mathrm{O}=\mathrm{XH}_2\mathrm{O}_{in}*f\mathrm{H}_2\mathrm{O}^o$ where $f\mathrm{H}_2\mathrm{O}^o$ is the fugacity of pure water. Afterwards, the $f\mathrm{O}_2$ for each capsule was calculated and the results are shown in Table 2.

A series of experiments was performed at 850 and 800ºC under oxidizing conditions with oxygen fugacities equivalent to NNO±0.5; whereas another series of experiments was mainly performed at 850ºC and reducing conditions with $f\mathrm{O}_2$ equivalent to FMQ±0.5 (Table 2). In both cases $f\mathrm{O}_2$ varies with temperature and decreasing a$\mathrm{H}_2\mathrm{O}$ (or $\mathrm{XH}_2\mathrm{O}_{in}$) at given temperature and pressure as expected (e.g., Scaillet et al., 1995; Berndt et al., 2005; Freise et al., 2009). In water-undersaturated charges, the decrease in $\mathrm{XH}_2\mathrm{O}_{in}$, hence in $f\mathrm{H}_2\mathrm{O}$, produces a decrease in $f\mathrm{O}_2$, because of the dissociation reaction of water as the following equilibrium shows:

$$\mathrm{H}_2\mathrm{O} = \mathrm{H}_2 + \tfrac{1}{2}\,\mathrm{O}_2$$
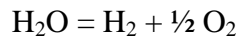
whose constant, K_{water}, writes as:

$$\log \mathrm{K}_{water} = \log f\mathrm{H}_2 + \tfrac{1}{2} \log f\mathrm{O}_2 - \log f\mathrm{H}_2\mathrm{O}$$

or

$$\log f\mathrm{O}_2 = 2\,(\log \mathrm{K}_{water} - \log f\mathrm{H}_2) + 2 \log f\mathrm{H}_2\mathrm{O}$$

assuming that $f\mathrm{H}_2\mathrm{O} = \mathrm{XH}_2\mathrm{O}_{in}*f\mathrm{H2O}°$, $f\mathrm{H}_2\mathrm{O}°$ being the fugacity of pure water at any given P and T, it follows that:

$$\log f\mathrm{O}_2 = 2\,(\log \mathrm{K}_{water} - \log f\mathrm{H}_2) + 2\,(\log f\mathrm{H}_2\mathrm{O}°) + 2\,(\log \mathrm{XH}_2\mathrm{O}_{in})$$

It is apparent that, at fixed $f\mathrm{H}_2$, if $f\mathrm{H}_2\mathrm{O}$ decreases, then $f\mathrm{O}_2$ must decrease, because the last rightward term of the above equation is necessarily a negative quantity. Therefore, if a water saturated charge (ie $\mathrm{XH}_2\mathrm{O}_{in}=1$) is ran with an $f\mathrm{H}_2$ corresponding to an $f\mathrm{O}_2=$NNO (or FMQ), anyother one ran with $\mathrm{XH}_2\mathrm{O}_{in}<1$, will have an $f\mathrm{O}_2 <$ NNO (or < FMQ for more reduced experiments; Table 2). An $\mathrm{XH}_2\mathrm{O}_{in}=0.5$ imposes a corresponding decrease in $f\mathrm{O}_2$ of about 0.3 log unit, whilst with $\mathrm{XH}_2\mathrm{O}_{in}=0.2$, the decrease in $f\mathrm{O}_2$ is = 0.7 log unit. As a result, the obtained values for the two series of experiments overlap to some extent (i.e., Mg# in clinopyroxene and biotite, see below), because NNO and FMQ buffers differ by only 0.7 log unit (ie charges with low $\mathrm{XH}_2\mathrm{O}_{in}$ in a nominal NNO run will approach FMQ redox conditions). However, the differing mineral assemblages and phase compositions obtained in each series (e.g, presence of ilmenite+magnetite in oxidizing experiments, presence of only ilmenite under reduced conditions) bear evidence that we have successfully achieved different oxidation conditions in our two

set of experiments. Therefore, in the following, for simplicity, experiments conducted under oxidizing conditions will be referred to as NNO experiments whilst those conducted under slightly more reduced conditions will be referred to as FMQ experiments.

Analytical techniques

Experimental phases were analysed using a Cameca SX-50 electron microprobe with an acceleration voltage of 15 kV, a sample current of 6nA, and a counting time of 10s. For glasses, a defocused beam of 10 μm was used whereas for minerals a focused beam was employed. Alkali migration in glasses was quantified and corrected using secondary phonolitic standards with a composition similar to the natural obsidian and with dissolved water contents of 10 wt%, 6 wt% and 1.5 wt% respectively (Andújar et al., 2008, 2010).

Attainment of equilibrium

We have only conducted crystallization experiments in this work and we have not attempted to perform reversal experiments. However, the following lines of evidence suggest that our experiments closely approached equilibrium conditions: (i) the homogeneous distribution of the phases within the charges, (ii) the presence of euhedral crystals, (iii) the homogeneous phase compositions, including glasses (Fig. 2c), and (iv) the fact that, phase proportions and compositions vary smoothly with changes in experimental conditions. The duration of our experiments (1 to 2 weeks) is within the range of that of other studies, including for phonolitic systems (Berndt et al., 2001; Freise et al., 2003; Harms et al., 2004; Scaillet et al., 2008), for which close to equilibrium conditions have been claimed (see also Scaillet & Evans 1999; Costa et al., 2004; Andújar et al., 2008, 2010, and Pichavant et al., 2007).

RESULTS

Phase assemblages are given in Table 2. Phase proportions were obtained by mass-balance calculations using the bulk rock composition and the composition of the phases present in the charge.

Identified mineral phases in are: alkali feldspar, biotite, magnetite, ilmenite, clinopyroxene and titanite, this last appearing only at 800ºC and 200 MPa. Typically, alkali feldspar and clinopyroxene at 800ºC have larger sizes (>100μm) than those at

850ºC (< 10μm). Whenever possible, at least 5 analyses per phase were done: however, in charges with small crystal sizes (< 10μm) it was difficult to obtain electron microprobe analysis without glass contamination, in particular for clinopyroxene which often displayed K_2O contents higher than 0.1 wt%. In this case, the glass contribution was calculated out by assuming a zero content of K_2O in clinopyroxene. Although such a procedure may introduce compositional biais, we note that: a) substracted amounts of glass are < 20%; b) the standard deviation of each restored composition remains very low, except in two charges (MB21 and MB117) where the error associated to Al_2O_3 is similar to that of the non-restored composition; c) mineral analyses agree with the structural formula of clinopyroxene; d) residuals from mass-balance calculations in experiments where clinopyroxenes analyses have been re-calculated are commonly < 0.5; e) the variation of restored clinopyroxene composition (Mg#, En, Fs, Wo) with intensive parameters (T, P, aH_2O) is similar to that obtained in experimental studies performed on other phonolitic compositions (i.e., Vesivius, Tenerife, Laacher See, Kerguelen islands; Scaillet et al. 2008, Berndt et al. 2001, Freise et al. 2003, Andújar et al. 2008, 2010). We thus conclude that our procedure for correcting glass contaminated analyses reproduces satisfactorily the composition of experimental clinopyroxenes which can be used to gain information concerning the storage conditions of the phonolite.

Phase relations

We use a series of polybaric-isothermal (Fig. 5a-c) or isobaric-polythermal (Fig. 5d-e) sections to show the effects that changes in different variables (P, T, H_2O content and fO_2) have on phase relations.

At NNO and 850ºC (Fig. 5a,e) magnetite is the liquidus phase at all investigated pressures and water contents. With decreasing melt water contents (H_2O_{melt}) magnetite crystallization is followed by biotite, clinopyroxene and alkali feldspar, the latter phase appearing at H_2O_{melt} < 3-4 wt% depending on pressure (Fig. 5d,e). Ilmenite has a narrow stability field at these conditions, crystallizing at pressures <125MPa and H_2O_{melt} < 3 wt%. At NNO, a decrease of 50ºC increases the stability field of the all phases towards higher H_2O_{melt} (Fig. 5c), biotite being the liquidus phase, followed by magnetite and clinopyroxene, at H_2O_{melt} < 6.5 and 5.5 wt%, respectively. Ilmenite increases its stability to H_2O_{melt} between 4.5 and 5.5 wt% and co-crystallizes with alkali feldspar at 200MPa. At 800ºC titanite also crystallizes for H_2O_{melt} < 6 wt% at 200MPa

(Figs. 5c). The stability field of titanite is only broadly constrained as we have conducted experiments only at two different pressures: our results show that, under the T-fO_2 conditions explored, this phase only appears at pressures >150 MPa (Figs. 5c and 5d).

The phase relationships at FMQ, 850ºC and pressures ranging from 200 to 50 MPa are shown on Fig. 5b. It is apparent that a moderate decrease in fO_2 (from NNO to FMQ) increases biotite stability which becomes the liquidus phase, while magnetite is lacking. Clinopyroxene stability is slightly enlarged: it crystallizes after biotite and is followed by ilmenite whose stability is also increased towards higher pressure and H_2O_{melt} relative to that at NNO. Alkali feldspar appears after ilmenite and crystallizes at pressures and H_2O_{melt} similar to that at NNO.

Polythermal sections at 200 and 100MPa for redox conditions around NNO are shown on Fig 5d,e. At 200 MPa, biotite and magnetite crystallise first, followed by clinopyroxene, alkali feldspar, then ilmenite, at decreasing H_2O_{melt}. At 100 MPa the same order of crystallization is observed, the main difference being the lack of titanite (Fig. 5e).

Phase proportions

The crystal content varies systematically with temperature, H_2O_{melt}, pressure and oxygen fugacity. It increases with decreasing H_2O_{melt}. For a given H_2O_{melt}, the crystal content increases with either increasing pressure and oxygen fugacity or decreasing temperature. At 850ºC and for a given H_2O_{melt}, the decrease in oxygen fugacity from NNO to FMQ decreases the crystal content of the experimental charges, an effect which is more apparent at 50 MPa (Figs. 5a and 5b; Table 2). At water-saturated conditions biotite is the most abundant phase. Magnetite and clinopyroxene have similar abundances but are present in lower concentrations compared to biotite (generally <1 wt%, Table 2). However, the crystal content remains low in the charges (<5 wt%) until alkali feldspar crystallizes. Then, the crystallinity increases rapidly and alkali feldspar becomes the most abundant phase, as in the rock (Ablay et al., 1995).

Mineral compositions

Magnetite and ilmenite are present in the experimental charges but in only two of these was the size large enough for obtaining reliable electron microprobe analyses (ilmenite in run MB24: 50 wt% TiO_2, FeO*: 42wt%; magnetite run MB43: TiO_2: 16

wt%; FeO*: 78 wt%, Mg-number: 3.6). For the other charges magnetite/ilmenite were identified by SEM-EDS qualitative analyses.

Biotite

Representative analyses are given in Table 4. The Ti content in biotite increases slightly with decreasing H_2O_{melt} (Fig. 6a), although not reaching the Ti content of the biotite phenocryst. The Mg# of experimental biotites ranges between 40 and 59, depending essentially on fO_2, with FMQ charges plotting close to an Mg#=60 while those annealed at NNO yield Mg# between 40 and 50 (Fig. 6b).

Alkali feldspar

Alkali feldspars produced at 850ºC are anorthoclase with compositions in the range Ab_{61-65}, Or_{32-35}, An_{2-4} and display in general small compositional variation with experimental parameters (Table 5; Fig 7). They encompass the range of compositions recorded by the natural anorthoclase cores from the obsidian (An_{2-4}). In experiments conducted at 800ºC, 200MPa, and NNO, the feldspar crystallising is a sanidine (Ab_{50-63}, Or_{36-49}, $An_{1.3-1.5}$). When temperature decreases from 850 to 800°C, An decreases from 3.5 to 1.5 mole%, Ab from 65 to 50 mole% whereas Or increases from 35 to 50 mole%, in accord with previous experimental results for similar bulk rock compositions (e.g., Andújar et al. 2008, 2010).

Clinopyroxene

Clinopyroxene compositions are shown in Table 6. All experimental clinopyroxenes crystallizing at 850ºC are diopside (Fig. 8a; Morimoto, 1989) with compositions in the range En_{30-35}, Fs_{18-22}, Wo_{44-47} and Mg# = 58-66, closely approaching natural compositions. Clinopyroxenes from experiments conducted at 800ºC, 200 MPa and NNO are hedenbergite (En_{24-25}, Fs_{27-28}, Wo_{46-47}) with a Mg# lower than at 850°C, between 46-47 (Fig. 8). At 50 MPa, 850°C and $H_2O_{melt} < 2.8$wt%, a decrease in fO_2 from NNO to FMQ increases the Mg# from 57 to 65, a trend opposite to that expected (a decrease in fO_2 decreases the Mg# of clinopyroxenes; Freise et al., 2003; Costa et al., 2004), though the magnitude of the change remains small. The Wo content does not show any appreciable variation with H_2O_{melt}, in contrast to observations made in silicic to intermediate calc-alkaline magmas (e.g., Scaillet & Evans, 1999).

Glass

Experimental glasses are phonolitic in composition and slightly to moderately per-alkaline [Na_2O+K_2O between 15 and 17 wt%; molar (Na+K/Al) between 1.1 and 1.3] with SiO_2 contents between 58.8 and 61.5 wt% (compositions re-calculated to 100% anhydrous; Table 7; Fig. 9). Experimental glass composition varies according to changes in experimental parameters (Fig. 9), though changes relative to the starting composition remain moderate owing to the generally low crystallinity of the charges. For a given pressure and temperature, a decrease in H_2O_{melt} decreases SiO_2, CaO, TiO_2 and increases MgO, Na_2O and K_2O. The effect of temperature can be observed at 200 MPa where a decrease of 50ºC in temperature produces a decrease in CaO, FeO*, TiO_2 and MgO contents whereas SiO_2 increases. A reduction of fO_2 from NNO to FMQ produces slight but detectable changes in several oxides (Fig. 9). In general, however, apart from the 800°C-200MPa-NNO group, the modest magnitude of changes of many oxides prevent from using glass composition as a tool for inferring rigorously either pre-eruptive magmatic H_2O_{melt} or fO_2. Only the variations of CaO contents seem to suggest pre-eruptive H_2O_{melt} in the range 2-3 wt%.

These compositional variations with temperature, H_2O_{melt} and oxygen fugacity are in general agreement with those observed in previous works on phonolitic and calc-alkaline compositions (e.g., Berndt et al., 2001; Freise et al., 2003; Andújar et al., 2008, 2010; Costa et al., 2004). However, experiments conducted at 50 MPa display a behaviour different than those conducted at higher pressures where CaO, MgO and FeO* content increases with decreasing water content in the melt. As mentioned above, the Mg# of experimental clinopyroxenes crystallizing at 50 MPa and at FMQ have higher Mg# than those crystallizing at NNO. The Mg# of Fe/Mg minerals depends on changes in temperature and/or fO_2 but also on the MgO content of the melt from which it precipitates. Figure 9 shows that experiments at 50 MPa produce residual melts with higher MgO content than at higher pressures. Moreover, when H_2O_{melt} decreases the MgO content increases, while at higher pressure the MgO content of the liquids does not change significantly with crystallization. As a result, glasses of charges ran at FMQ have slightly lower FeO*/MgO ratio than those of experiments performed at NNO (Fig. 9). We interpret such a peculiar Mg enrichment of low pressure charges as resulting from changes in phase abundances, in particular that of ilmenite at low fO_2, which forces coexisting phases to be Mg-richer at low fO_2 as compared to high fO_2.

DISCUSSION

Montaña Blanca phase relationships compared to other phonolites from Tenerife

Phase equilibrium experiments are performed with the aim of constraining the storage conditions of target eruptions with a representative composition. The results obtained from a specific composition can be potentially extrapolated to other eruptive events from the same volcano or from other volcanoes, as long as eruptive products are compositionally close to the studied sample. However, the general terms used for rock classification (e.g., dacite, rhyolite, phonolite; Le Maitre et al., 1989) encompass compositions displaying large differences in some major elements (CaO, MgO, Na_2O, K_2O) and therefore the generalisation of the results from phase equilibrium experiments must be done carefully. Indeed, small differences in bulk-rock composition have been shown to strongly affect the stability domains of key minerals (e.g., Scaillet et al., 2008). As we illustrate below, this is the case of Tenerife phonolites as well.

Experimental works on Tenerife are few, and apart from the work of Andújar et al. (2010) on Lavas Negras phonolitic eruption, there is only the study of Andújar et al. (2008) who constrained the pre-eruptive conditions for the last caldera-forming eruption of the island (El Abrigo eruption), which occurred ~200 000 yrs ago generating about 20 km^3 DRE of pyroclastic products (Edgar et al., 2007). The phonolites of El Abrigo and Lavas Negras have very similar Na_2O+K_2O contents which varies between 14.4 to 15.6 wt% and Montaña Blanca lies in between these two values (15.4), being very close to El Abrigo composition. If MgO content is taken as an indicator of magma evolution, both Montaña Blanca and El Abrigo are more evolved than the Lavas Negras phonolite (0.55 MgO wt%, Andújar et al., 2008, 2010). However, despite the seemingly small compositional differences between these three phonolites there exists considerable variations in their respective phase equilibria.

Phase relationships of El Abrigo (Andújar et al., 2008) show that alkali feldspar has a lower thermal stability as compared to Montaña Blanca, whereas titanite, which only appears at pressures >150MPa and <825ºC in Montaña Blanca, has a wider stabilibity field, possibly as the result of higher fO_2 explored for El Abrigo eruption (NNO+1). Several differences can be found for other accessory minerals. Ilmenite has a restricted stability field at 850ºC in the Montaña Blanca whereas in El Abrigo this phase is absent, again as a consequence of higher imposed fO_2. Haüyne is present in El Abrigo and has a pressure dependent stablility field, while it is absent in Montaña Blanca. Such

differences are due to somewhat lower CaO, FeO*, TiO$_2$ (differences between 0.1 to 0.5 wt%, Andújar et al., 2008) of El Abrigo bulk rock composition, in addition to the effects of volatile species such as S or Cl (and fO$_2$). The slightly more mafic character of Lavas Negras translates into overall higher temperatures for alkali feldspar, titanite and clinopyroxene crystallization, as compared to both El Abrigo and Montaña Blanca phonolites, hence increasing the crystal content of the corresponding magma when held at the same conditions of temperature and pressure (Andújar et al., 2010). We thus conclude that the extrapolation of experimental data to other compositions for constraining the storage conditions of the magma must be done with caution, paying particular attention to the role of fO$_2$.

Pre-eruptive conditions of Montaña Blanca eruption

A first constraint on the pre-eruptive conditions can be made by comparing the crystal content and mineral assemblage of the natural phonolite with those determined in the experiments. The assemblage alkali feldspar, biotite, magnetite, ilmenite and clinopyroxene has been reproduced only at 850ºC-NNO, 50±20 MPa and for H$_2$O$_{melt}$ of 2.5-3 wt%. However, the crystal content is generally higher at these conditions (> 5 to 15 wt%, Fig.5a) compared to the rock (5 wt%). Experiments performed at the same P-T-H$_2$O$_{melt}$ but lower fO$_2$ (FMQ), reproduce the crystal content and phase assemblage of the phonolite apart from magnetite which is absent (Fig.5b). At 800ºC-NNO the crystallization of the main mineral phases takes place at higher H$_2$O$_{melt}$ compared to experiments performed at 850ºC. At this temperature the natural assemblage can be reproduced in the pressure range 100-150 MPa for H$_2$O$_{melt}$ of ~4.5 wt% but at such conditions the crystal content is >10 wt%, which is higher than that of the natural sample (5wt%; Fig. 5). At 800ºC, pressures <100MPa can be ruled out as the crystal content would be >10 wt.% whereas at pressures >150 MPa titanite crystallizes, whilst it is absent in our starting rock as in most phonolites from Pico Teide (Ablay et al., 1998). Thus, 800ºC can be ruled out as pre-eruptive temperature as the crystal content is too high. Based on phase equilibrium considerations, we conclude that the pre-eruptive conditions are in the range 850±20ºC, 50±20MPa, H$_2$O$_{melt}$ of 2-3 wt% and fO$_2$ between NNO and FMQ.

The compositions of minerals confirm this first estimate. Experimental feldspars at 850°C are similar to those natural with no obvious correlation with H$_2$O$_{melt}$ (Fig. 7b). The natural biotite has an Mg# ~58 which is reproduced in the range of the determined

pre-eruptive conditions (Fig 6b). In contrast, the Ti content of the natural biotite (~0.38 a.p.f.u) is slightly higher than experimental biotites crystallizing around FMQ (Fig. 6a). This could reflect that the natural phonolite was either at a temperature slightly higher than 850ºC or, and more likely, that the fO_2 was higher than FMQ, as already suggested above. A slightly higher fO_2 would lead to a lower amount of ilmenite, allowing more Ti to be taken up by co-existing biotite. The natural clinopyroxene has a composition $En_{36}Fs_{16}Wo_{45}$ and a Mg# of 68 which is slightly higher than those of clinopyroxenes crystallizing at the previously constrained pre-eruptive conditions. As for biotite, this suggests crystallization at somewhat higher temperature and/or fO_2. The fact that the natural biotite, clinopyroxene and crystallinity are broadly reproduced between NNO and FMQ points to an fO_2 between such buffers (~NNO-0.4), in accord with previous work on other phonolites from Tenerife (Ablay et al., 1998, Andújar et al., 2008, 2010).

We have not conducted experiments at temperatures higher than 850ºC but we consider that the pre-eruptive temperature at 850±15ºC is the most likely one because (1) it reproduces the dominant composition of alkali feldspar (An_{2-4}), (2) it reproduces the Mg# of natural biotite which is highly sensitive to temperature (e.g. Berndt et al., 2001; Freise et al., 2003), and (3) it matches with independent Fe-Ti oxides constraints which gives a temperature range of 835-865ºC (Ablay et al., 1995; 1998). Experimental works conducted on similar phonolitic compositions (Andújar et al., 2008, 2010), show that a temperature of 875-900°C would give Mg-rich biotite (Mg#=70) and yield an alkali feldspar with 5-6% An and 30% Or, which are not found in the rock (Fig. 3).

On the basis of the above lines of evidence we conclude that the pre-eruptive conditions of the Montaña Blanca main phonolite are 850±15ºC, 50±20MPa, 2.5±0.5wt% H_2O, and fO_2 between NNO and FMQ.

Mineralogical evidence for a deep reservoir and magma mixing

There are, however, some minor attributes that are not reproduced at such conditions. Firstly, some feldspar phenocrysts have distinctly An poorer compositions. Secondly, some clinopyroxene have melt inclusions with H_2O_{melt} higher than 3 wt% (Ablay et al. 1995). Thirdly, the outer rim of alkali feldspar is clearly different from phase compositions obtained under such conditions. Possible explanations of such features are listed below.

An-poor alkali feldspar

At 800°C and 200 MPa, the experimental feldspar matches some of the alkali feldspar phenocrysts cores with An contents < 2, though such conditions reproduce neither the phase assemblage, nor the majority of mineral and glass compositions of the phonolite. Such core compositions suggest a low temperature origin for these alkali feldspars, compatible with pre-eruptive temperature information obtained for some other Montaña Blanca units using Fe-Ti oxide pairs (e.g., UMB III yields temperatures of 775ºC). Ablay et al. (1995) proposed that the Montaña Blanca magma reservoir (Fig. 1b) is thermally and compositionally zoned, with the coldest unit UMBIII phonolite capping the reservoir, underlain by the unit UMBII magma. We suggest that the colder and top phonolite is the source of the An < 2 compositions, whereas those with composition An_{4-2} crystallized from the main body of phonolite studied in this work. The trace element geochemistry of the erupted sequence reveals the existence of compositional gaps between the phonolitic products co-existing in the magmatic reservoir suggesting that these magmas were separated by sharp interfaces (Ablay et al., 1995). The thermal contrast between the two phonolites could have generated a convective process leading to the entrainment of some An-poor crystals into the main phonolite (Fig. 3).

Clinopyroxene with water-rich melt inclusions

Water contents in melt inclusions trapped in some clinopyroxenes of the Montaña Blanca products are in the range of 3 to 4.5 wt% with a single extreme value of 6.5 wt%H_2O (Ablay et al., 1995). The composition of such melt inclusions in clinopyroxene is unfortunately unknown, which prevents from any conclusive statement on their origin (Ablay et al., 1995). Yet, crystallization at 850ºC, 100 MPa, either FMQ or NNO, and water contents of 3.5 wt% yield clinopyroxene compositions close to those of the natural obsidian (Fig. 8). This suggests that some clinopyoxenes could have crystallized at slightly deeper conditions, from a melt with higher water contents than that inferred above. Considering the available literature data on the magmatic system of Teide - Pico Viejo volcanic complex, a possible deeper source for these clinopyroxenes is the magmatic reservoir of Teide that has been constrained to be at 5 km (Andújar et al., 2010). This phonolite has clinopyroxene phenocrysts with composition En_{37} Fs_{15} Wo_{47} that indeed resemble that of the Montaña Blanca phonolite (Table 1). Thus, some Montaña Blanca clinopyroxenes could be remnants of the injection of a deeper phonolite stored at the same level as the main Teide magmatic reservoir. This would

imply that such a reservoir, which was tapped during the Lavas Negras event some 1 ky ago, was already present during the MB event.

Alkali feldspar rim and microlite

All alkali feldspar phenocrysts are characterised by anorthite-rich and orthose-poor overgrowths with a composition close to that of the microlite (Fig. 3). Our results show that such Ca- Fe- rich overgrowths and microlites cannot be produced under the pre-eruptive conditions established here. Traditionally such features are interpreted as arising from magma mixing (e.g., Couch et al., 2001; Martel et al., 2006). However, recent experimental studies provide alternative explanations, or elaborations, to that general interpretation: 1) changes in mineral composition due to extensive decompression-driven crystallisation during magma ascent and accompanying latent heat release that increases temperature (Blundy et al., 2006), 2) re-heating of the system by mafic magma underplating of the reservoir (Couch et al,. 2001; Triebold et al., 2006), 3) mafic microlites entrainment into the felsic reservoir (Martel et al., 2006).

A decompression-driven heating mechanism seems, however, unlikely in view of the Plinian context of the Montana Blanca eruption, which is characerised by high magma ascent rates that inhibit crystallization (e.g., Castro & Gardner 2008). The second possibility, proposed by Couch et al. (2001) for the Soufriere Hill volcano, explains the presence of mafic microlites by a process of self-mixing in open magma chambers. In such a self-convective model, the thermal difference originated by the underplating of a hot mafic magma of a felsic reservoir generates vigorous convective cells that enable the mixing of magma with a similar composition. Such a model does not require a mass transfer between the felsic and the mafic components. However, detailed back-scattered images of the alkali feldspars from the natural obsidian do not reveal the presence of a re-absorption surface before the An–rich overgrowth (Fig.2), which are expected during re-heating of magma parcels entrained in convective cells.

The third possibility has been proposed by Martel et al. (2006) and Humphreys et al. (2010) for Mt Pelée and Soufriere Hill volcanoes, respectively. These authors explained the presence of An-rich microlites and Ca-rich plagioclase as the result of discrete mafic melt intrusions into an andesitic magma. Such a process would also explain the rimwards enrichment in FeO* content, from 0.1-0.3 wt% to 0.9-1.6 wt% FeO* (Fig. 3), as documented at Teide or in other systems where mixing has been argued (e.g., Triebold et al. 2006; Ruprecht & Wörner, 2007; Humphreys et al. 2010).

The banded pumices found at the top of unit UMBII have been interpreted as resulting from injection of mafic magma into the system during or just prior to eruption (Ablay et al., 1995). We thus suggest that a process of magma mixing is the more likely mechanism for explaining An-rich rims and microlite composition.

The abrupt An zonation of the rims further suggests that the two magmas were in contact for a short period of time before eruption. The lack of zoning in other phenocrysts can be also explained by very short time exposure to new conditions (e.g., Cherniak & Dimanov, 2010). On this basis, we suggest that the mixing process mostly occurred close to the boundary layer that separated the two magmas, probably owing to magma injection shortly before eruption. Such a mixing may have triggered the Montana Blanca eruption.

Further insight on the plumbing system of Teide volcanic complex and on its role on eruptive dynamics

The volcanism of the last 3000 yr of Teide volcano is characterised predominantly by an effusive or transient explosive phonolitic magmatism (Ablay & Martí, 2000; Martí et al., 2008), with a single plinian event, the Montaña Blanca eruption, which occurred from a lateral vent of the system rather from the Teide proper. The constancy in composition over the last 3000 yr (Ablay et al., 1998) suggests that differences in eruptive styles may be related to differences in pre/syn-eruptive conditions (i.e. Martel et al., 1998). The storage conditions of the last central eruption of Teide (i.e., Lavas Negras, 1150 years ago, with about 0.5 km^3 of lavas (Ablay & Martí, 2000)), have been determined by Andújar et al. (2010). The phonolitic magma contained about 30-40 vol% phenocrysts and was stored at 5 km depth, 900ºC and with 3 wt% H_2O_{mel}, which are somewhat hotter and wetter, but clearly deeper conditions than those inferred for the Montana Blanca reservoir. As Teide pre-eruptive paleo surface before the last eruption has been determined to be at heights of 3500 m a.s.l. (Carracedo et al. 2007; Ablay & Martí 2000), the magmatic reservoir that fed central Teide phonolitic eruptions can be placed at 1.5 km below sea level (Fig. 10; Andújar et al. 2010). In contrast, since the plinian phase of the Montaña Blanca eruption occurred from a vent located at 2500-2700 m a.s.l. (Carracedo et al. 2007; Ablay et al. 1995), this eruption tapped a reservoir located at ~1000 m above the sea level, according to our pressure estimate (Fig. 10). Hence, such a difference in depths suggests that, by the time of the MB plinian phase, two main levels of magma ponding existed, being separated by

about 2.5 km depth (Fig. 10). Whether such levels are parts of a single elongated reservoir, or form discrete pockets relatively isolated from each other, such as illustrated on Fig. 10, remains unknown.

Such differences in the petrological characteristics and storage conditions between central Teide and Montaña Blanca phonolites can impart differences in the rheological behaviour of the magmas (i.e, viscosity). In particular, the fact that MB and Teide magmas had similar pre-eruptive H_2O_{melt} (~3 wt%), suggests that one factor controlling the difference in the eruptive behaviour might be the difference in storage pressure, which defines the proximity of such magmas to water-saturated conditions (i.e., bubble nucleation in absence of other volatiles). The pre-eruptive water contents of these eruptions are both around 3 ± 1 wt% H_2O, which implies that water-saturation is achieved at pressures of about 50 MPa (Fig. 5). Hence, in the case of Pico Teide, the magma has to travel a distance of 3 km before achieving H_2O-saturation. During this journey to the surface, the ascending magma can experience an increase in viscosity (Martel & Schdmit, 2003; Castro & Gardner, 2008), owing to microlite crystallization, which slows magma ascent within the conduit. By the time H_2O-saturation is reached, the viscosity of magma may be large enough to greatly inhibit its explosive potential (e.g., Castro & Mercer, 2004; Castro & Gardner, 2008), thereby promoting an effusive regime. In contrast, in the case of Montaña Blanca, the level of storage is close enough to water-saturation so as to allow bubble growth and coalescence in the reservoir which ultimately thus favouring an explosive activity (Larsen & Gardner, 2004; Iacono Marziano et al., 2007). This may explain why despite having similar composition and water contents, Teide magmas erupted effusively, whereas Montaña Blanca erupted explosively. It must be noted that such a model implicitly assumes that other volatiles, in particular CO_2, were not present in any significant abundance in the system.

The Montaña Blanca eruption compared to other phonolitic eruptions

Several experimental studies have been performed in phonolitic volcanoes that have produced plinian eruptions during the Holocene. For example one of those is the Somma-Vesuvius volcanic system that has experienced several caldera collapses and produced important volumes of fall and pyroclastic material (Cioni et al., 1999). The storage conditions of several Plinian eruptions from this volcanic system have been experimentally constrained to be 200 ± 20 MPa, <750-825ºC and water contents of ca. 6 wt% (Scaillet et al., 2008). Hence, the phonolitic magmas of the Neapolitan region were

stored at deeper levels, lower temperatures and contained higher water contents than the Montaña Blanca magmas. The phonolitic volcanism of the Laacher See complex (Rhine Valley; e.g, Wörner & Schimncke, 1984) provides an additional example for understanding this type of volcanism. Harms et al. (2004) determined the pre-eruptive conditions for the most evolved phonolite of that system to be 130±15 MPa, 750-760ºC and 5-6wt% H_2O whereas magmas from deeper parts of such a magma reservoir where stored at 200 MPa (Berndt et al., 2001). The Laacher See phonolite was thus stored at higher depths and contained more water than Montaña Blanca. Application of solubility models for phonolitic melts (Carroll & Blanck, 1997; Schmidt & Behrens, 2008) shows that the three systems were close to water-saturation (Vesuvius and Montaña Blanca) or even at water-saturated conditions (Laacher See). This may explain why these systems, while stored at different depths and with different water contents, displayed similar eruptive dynamics, ie the generation of powerfull Plinian eruptions. In contrast, phase equilibrium experiments performed on phonolitic lavas from Kerguelen Islands and Tenerife (Freise at al. 2003; Andújar et al., 2010) show that such effusive-transient explosive phonolitic magmas were water-undersaturated at their storage conditions (5 wt%, 225 MPa for Kerguelen lavas; 3 wt%, 150 MPa for Teide). The compilation of data presented in the this work thus suggests that sustained explosive eruptions are sourced from storage regions at or close to H_2O-saturation, whilst effusive events began their ascent under markedly under-saturated conditions. Clearly, however, the still limited data base on plinian and effusive phonolitic eruptions, makes it necessary to gain further information concerning storage conditions and volatile contents on these magmas before any conclusive statement can be made.

CONCLUSIONS

The combination of the petrological observations, phase relations, mineral and melt compositions of the natural and experimental products of the Montaña Blanca eruption has allowed us to constrain the conditions of storage of the phonolitic magma and the structure of the magmatic reservoir before the eruption. The Unit II magma that generated the sub-plinian event of the Montaña Blanca eruption was stored at 850±15ºC, 50±20MPa, 2.5±0.5wt% dissolved H_2O, and fO_2 between NNO and FMQ. At such conditions we have reproduced the phenocryst content (5 wt%), the mineral assemblage and most of the phase compositions of the natural phonolite. The

composition of some feldspar, are in contrast reproduced only in experiments conducted at 100MPa suggesting crystallization at deeper conditions for part of this mineral phase. Pressures of at least 100 MPa are indicated by H_2O_{melt} found in melt inclusions of clinopyroxenes (Ablay et al., 1995). Just prior to the eruption, an injection of mafic magma occurred in the reservoir, a process that was recorded in the alkali feldspars phenocrysts by An rich rims and in the matrix, by the crystallization of microlites having the same composition than the feldspars rims. This mafic intrusion could have triggered the eruption of the phonolitic magma leading to the sub-plinian eruption of Montaña Blanca.

The comparison with experimental results on other phonolites from Teide volcano has allowed us to shed light on the parameters that govern the eruptive dynamic of phonolitic magmas in Tenerife during the last 3000 yrs, in particular pressure, which controls the proximity of the magma to water-saturation and hence, the rheological properties and ensuing eruptive dynamics of the magma.

The comparison of our results from phonolitic eruptions indicates that explosive events can occur from magmatic reservoirs located between 1 to 6 km depth but that near water-saturation conditions seem to be required for explosive eruptions to occur.

References

Ablay, G. J., Ernst, G. G. J., Martí, J. & Sparks, R.S.J. (1995). The 2ka subplinian eruption of Montaña Blanca, Tenerife. *Bulletin of Volcanology* **57,** 337-355.

Ablay, G. J., Carroll, M.R., Palmer, M.R., Martí, J. & Sparks, R.S.J. (1998). Basanite-Phonolite Lineages of the Teide-Pico Viejo Volcanic Complex, Tenerife, Canary Islands. *Journal of Petrology* **39**, 905-936.

Ablay, G. J. & Martí, J. (2000). Stratigraphy, structure, and volcanic evolution of the Pico Teide-Pico Viejo formation, Tenerife, Canary Islands. *Journal of Volcanology and Geothermal Research* **103**, 175-208.

Ancochea E., Fúster J.M., Ibarrola E., Cendrero, A., Coello, J., Hernán, F., Cantagrel, J.M. & Jamond, C. (1990). Volcanic evolution of the island of Tenerife (Canary Islands) in the light of new K-Ar data. *Journal of Volcanology and Geothermal Research,* **44**, 231-249.

Andújar, J., Costa, F., Martí, J., Wolff, J.A. & Caroll, M.R. (2008). Experimental constraints on pre-eruptive conditions of phonolitic magma from the caldera-forming El Abrigo eruption, Tenerife (Canary islands). *Chemical Geology* **257**, 173-191

Andújar, J., Costa, F.& Martí, J. (2010). Magma storage conditions of the last eruption of Teide volcano (Canary Islands, Spain). *Bulletin of Volcanology* **72**, 381-395.

Araña, V. (1971). Litología y estructura del Edificio Cañadas, Tenerife (Islas Canarias). *Estudios Geologicos* **27**, 95-135.

Berndt, J., Holtz, F. & Koepke, J. (2001). Experimental constraints on storage conditions in the chemically zoned phonolitic magma chamber of the Laacher See volcano. *Contributions to Mineralogy and Petrology* **140**,469-486

Berndt, J., Koepke, J. & Holtz, F. (2005). An experimental investigation of the influence of water and oxygen fugacity on differentiation of MORB at 200 MPa. *Journal of Petrology* **46**, 135-167.

Blundy, J., Cashman, K. & Humphreys, M. (2006). Magma heating by decompression-driven crystallization beneath andesite volcanoes. *Nature* **443**, 76-80

Carracedo, J.C. & Rodríguez-Badiola (2006). Los domos y domos-colada del complejo volcanico del Teide in:Carracedo JC, ed: Los volcanes del parque nacional del Teide: Madrid, serie técnica.

Carracedo, J.C., Rodríguez-Badiola, E., Guillou, H., Paterne, M., Scaillet, S., Pérez-Torrado, F. J., Paris, R., Fra-Paelo, U. & Hansen, A. (2007). Eruptive and structural history of Teide volcano and rift zones of Tenerife, Canary Islands. *Geological Society American Bulletin* **119**, 1027-1051

Carroll, M. R. & Blank, J.G. (1997). The solubility of H_2O in phonolitic melts. *American Mineralogist* **82**, 549-556.

Castro, J.M. & Mercer, C. (2004). Microlite textures and volatile contents of obsidian from Inyo volcanic chain, California. *Geophysical Research Letters* **31**, L18605.

Castro, J.M.& Gardner, J.E. (2008). Did magma ascent rate control the explosive-effusive transition at the Inyo volcanic chain, California? *Geology* **36**, 279-282.

Cherniak, D.J. & Dimanov, A. (2010). Diffusion in pyroxene, mica and amphibole. *Reviews in Mineralogy and Geochemistry* **72**, 641-690.

Cioni, R., Santacroce, R. & Sbrana, A. (1999). Pyroclastic deposits as a guide for reconstructing the multi-stage evolution of the Somma- vesuvius Caldera. *Bulletin of Volcanology* **60**, 207-222.

Costa, F., Scaillet, B. & Pichavant, M. (2004). Petrological and experimental constraints on the Pre-eruption conditions of Holocene dacite from Volcán San Pedro (36ºS, Chilean Andes) and the im portance of sulphur in silicic subduction-related magmas. *Journal of Petrology* **45,** 855-881.

Couch, S., Sparks, R.S.J. & Carroll, M.R. (2001). Mineral disequilibrium in lavas explained by convective self-mixing in open magma chamber. *Natur*e **441**,1037-1039.

Deer, W.A.; Howie, R.A. & Zussman, J. (1972). Rock forming minerals: Framework silicates **4**, 435 pp.

Di Carlo, I., Pichavant, M., Rotolo, S.G. & Scaillet, B. (2006). Experimental crystallization of a High-K arc basalt: the golden pumice, Stromboli volcano (Italy). *Journal of Petrology* **47**, 1317-1343.

Dymek, R. (1983). Titanium, aluminium and interlayer cation substitutions in biotite from the high-grade gneisses, West Greenland. *American Mineralogist* **68**, 880-899.

Edgar, C.J., Wolff, J.A , Olin, P.H., Nichols, H.J., Pittari, A., Cas, R.A.F., Reiners, P.W., Spell, T.L. & Martí, J. (2007). The late Quaternary Diego Hernandez Formation, Tenerife: Volcanology of a complex cycle of voluminous explosive phonolitic eruptions. *Journal of Volcanology and Geothermal Research* **160**, 59–85.

Freise, M., Holtz, F., Koepke, J., Scoates, J.& Leyrit, H. (2003). Experimental constraints on the storage conditions of phonolites from kerguelen Archipielago. *Contributions to Mineralogy and Petrology* **145**, 659-672.

Freise, M., Holtz, F., Nowak, M., Scoates, J.S. & Strauss, H. (2009). Differentiation and crystallization conditions of basalts from the Kerguelen large igneous province: an experimental study. *Contributions to Mineralogy and Petrology* **158**, 505-527.

Harms, E., Gardner., J.E. & Schmincke, H.U. (2004). Phase equilibria of the lower Laacher See Tephra (East Eifel, Germany): constrainsts on pre-eruptive storage conditions of a phonolitic magma reservoir. Journal *of Volcanology and Geothermal Research* **134**, 135-148.

Hausen, H. (1956). Contributions to the geology of Tenerife. *Societas Scientiarium. Fennica Commentationes Physico-Mathematicae* **18**, 1-247.

Humprheys, M. C.S., Edmonds, M., Christopher, T. & Hards, V. (2010). Magma hybridisation and diffusive exchange recorded in heterogeneous glasses from Soufrière Hills Volcano, Montserrat. Geophysical Research Letters **37**, L00E06, doi:10.1029/2009GL041926

Iacono Marziano, G., Schmidt, B.C. & Dolfi, D. (2007). Equilibrium and disequilibrium degassing of a phonolitic melt (Vesuvius AD 79 "white pumice") simulated by

decompression experiments. *Journal of Volcanology and Geothermal Research* **161**, 151-157.

Larsen, J.F. & Gardner, J.E. (2004). Experimental study of water degassing from phonolite melts: implications for volatile oversaturation during magmatic ascent. *Journal of Volcanology and Geothermal Research* **134**, 109-124.

Le Maitre, R.W., Bateman, P., Dudek, A., Keller, J., La Meyre Le Bas, M.J., Sabine, P.A., Schmid, R., Sorensen, H., Streckeisen, A., Wooley, A.R.& Zanettin, B. (1989). A classification of igneous rocks and glossary of terms. *Blackwell Scientific Publications*, 193 pp. Oxford.

Martel, C., Pichavant, M., Bourdier, J.L, Traineau, H., Holtz, F. & Scaillet, B. (1998). Magma storage conditions and control of eruption regime in silicic volcanoes: Experimental evidence from Mt. Pelée. *Earth and Planetary Science Letters* **156**, 89-99.

Martel, C., Pichavant, M., Holtz, F. & Scaillet, B. (1999). Effects of fO$_2$ and H$_2$O on andesite phase relations between 2 and 4 kbar. *Journal of Geophysical Research* **104**, 29,453-29,470.

Martel, C. & Schmidt, B.C. (2003) Decompression experiments as an insight into ascent rates of silicio magmas. *Contributions to Mineralogy and Petrology* **144**, 397-415.

Martel, C., Ali, A.R., Poussineau, S., Gourgaud, A. & Pichavant, M. (2006). Basalt-inherited microlites in silicic magmas: Evidence from Mount Pelée (Martinique, French West Indies). *Geology* **34**, 905-908.

Martí J., Mitjavila J. & Araña, V. (1994) Stratigraphy, structure and geochronology of the Las Cañadas caldera (Tenerife, Canary Island). *Geological Magazine* **131**,715-727

Martí J., Hurlimann M., Ablay G.J. & Gudmundsson, A. (1997) Vertical and lateral collapses on Tenerife (Canary Islands) and other volcanic ocean islands. *Geology* **25**, 879-882.

Martí, J. & Gudmundsson, A. (2000). The Las Cañadas caldera (Tenerife, Canary Islands): an overlapping collapse caldera generated by magma-chamber migration. *Journal of Volcanology and Geothermal Research* **103**, 161-173.

Martí, J., Geyer, A., Andújar, J., Teixidó, F. & Costa, F. (2008) Assessing the potential for future explosive activity from Teide-Pico Viejo. *Journal of Volcanology and Geothermal Research* **178**, 529-542

Moretti, R. & Papale, P. (2004). On the oxidation state and volatile behavior in multicomponent gas–melt equilibria. *Chemical Geology* **213**, 265-280.

Morimoto N. (1989). Nomenclature of pyroxenes. Subcomitee on pyroxenes. Commission on new minerals and mineral names. *Canadian Mineralogist* **27**, 143-156.

Morizet, Y., Brooker, R.A. & Kohn, S.C. (2002). CO_2 in haplo-phonolite melt: solubility, speciation and carbonate complexation. *Geochimicia et Cosmochimica Acta* **66**, 1809–1820.

Papale, P., Moretti, R. & Barbato, D. (2006). The compositional dependence of the saturation surface of H_2O+CO_2 fluids in silicate melts. *Chemical Geology* **229**, 78–95

Pichavant, M., Costa, F., Burgisser, A., Scaillet, B., Martel, C & Poussineau, S. (2007). Equilibration scales in silicic to intermediate magmas - Implications for phase equilibrium studies. *Journal of Petrology* **48**, 1955-1972

Pownceby, M.I. & O'Neill, H. St.C. (1994). Thermodynamic data redox reactions at high temperatures.III. Activity-composition relations in Ni-Pd alloys from EMF measurements at 850-1250 K and calibration of the NiO+Ni-Pd assemblage a redox sensor. *Contributions to Mineralogy and Petrology* **116**, 327-339.

Richet, P., Whittington, A., Holtz, F., Behrens, H., Ohlhorst, S. & Wilke, M. (2000). Water and the density of silicate glasses. *Contributions to Mineralogy and Petrology* **138**, 337-347.

Robie, R.A., Hemingway, B.S. & Fisher, J.R. (1979). Thermodynamic properties of minerals and related substances at 298.15 K and 1 bar (10^5 pascals) pressure and at higher temperatures. *US Geological Survey Bulletin* **1452**, 456.

Ruprecht, P. & Wörner, G. (2007). Variable regimes in magma systems documented in plagioclase zoning patterns: El Misti stratovolcano and Andahua monogenetic cones. *Journal of Volcanology and Geothermal Research* **165**, 142-162.

Sack, R.O. & Ghiorso, M.S. (1991). An internally consistent model for the thermodynamic properties of Fe-Mg-titanomagnetite-aluminate spinels. *Contributions to Mineralogy and Petrology* **106**, 474-505.

Scaillet, B., Pichavant, M. & Roux, J. (1995). Experimental crystallization of leucogranites magmas. *Journal of Petrology* **36**, 663-705.

Scaillet, B. & Evans, B.W. (1999). The 15 June 1991 eruption of Mount Pinatubo. I. phase equilibria and Pre-eruption P-T-fO$_2$-aH$_2$O. *Journal of Petrology* **40**, 381-411.

Scaillet, B., Pichavant, M. & Cioni, R. (2008). Upward migration of Vesuvius magma chamber over the past 20,000 years. *Nature* **455**, 216-219.

Schmidt, B.C. & Behrens, H. (2008): Water solubility in phonolite melts: Influence of melt composition and temperature, Chemical Geology **256**, 258–267

Sparks, R.S.J., Barclay, J., Jaupart, C., Mader, H.M. & Phillips, J.C. (1994) Physical aspect of Magmatic degassing I. Experimental and theoretical constraints on Vesiculation. In Volatiles in magmas (eds. M.R. Carroll and J.R. Holloway) **30**, 413-445.

Taylor, J.R., Wall, V.J. & Pownceby, M.I. (1992). The calibration and application of accurate redox sensors. *American Mineralogist* 77, 284-295.

Triebold, S., Kronz, A. & Wörner, G. (2006). Anorthite-calibrated backscattered electron profiles, trace elements, and growth textures in feldspars from the Teide-

Pico viejo volcanic complex (Tenerife). *Journal of Volcanology and Geothermal Research* **154**, 117-130.

Wörner. G. & Schmincke, H-U. (1984). Petrogenesis of the zoned Laacher See Tephra. *Journal of Petrology* **25**, 836-851.

Figure captions
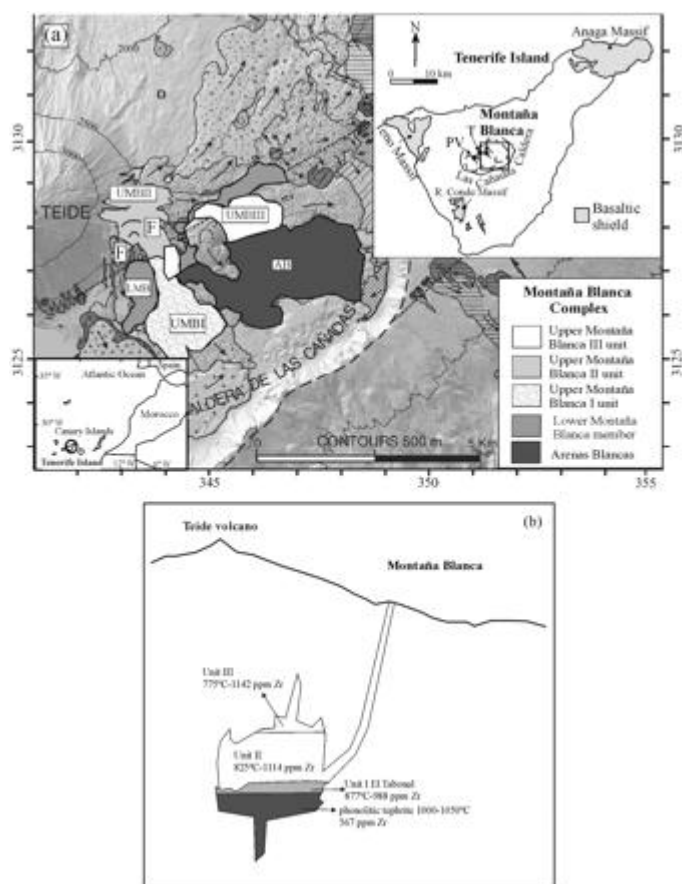
Figure 1. a) General situation of the Canary Islands and simplified geological map of the Montaña Blanca eruption (modified from Carracedo et al., 2007) showing the different members and sub-units according to Ablay et al. (1995). AB: arenas Blancas; LMB: lower Montaña Blanca member; UMBI: Upper Montaña Blanca I unit; UMBII: Upper Montaña Blanca II unit; UMBIII: Upper Montaña Blanca III unit; F: fissure-vents. Inner plate: geological map of Tenerife showing the products of the ancient basaltic shield, the las Cañadas Caldera depression and the actual volcanic complex of Teide (T), Pico Viejo (PV) and Motaña Blanca vent (Modified from Ablay & Martí, 2000). b) Schematic view of the Montaña Blanca reservoir prior to the eruption (modified from Ablay et al. 1995).
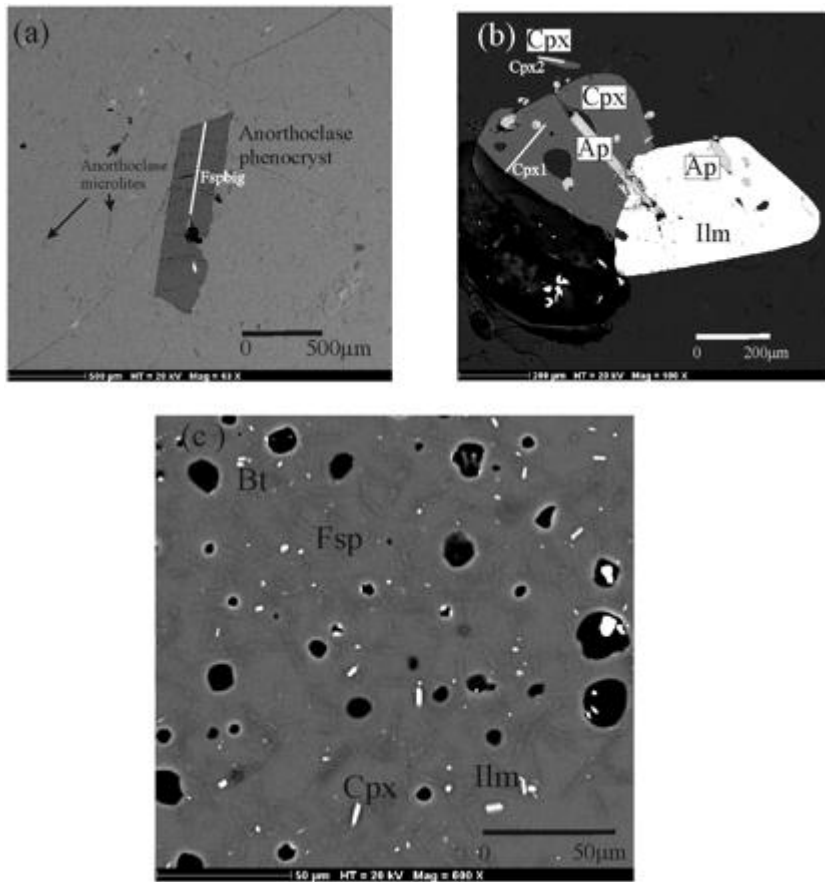
Figure 2. Back scattered SEM image of the natural obsidian a) showing Anorthoclase phenocrystal and Ca-rich microlites; b) showing phenocrysts of ilmenite (ilm) and diopside (cpx) containing inclusions of apatite (ap).White lines in plate a and b indicate the EMPA compositional profile of the mineral phases. C) Back scattered SEM image of an experimental charge that contains biotite (bt), diopside (cpx), alkali feldspar (fsp) and ilmenite (ilm).
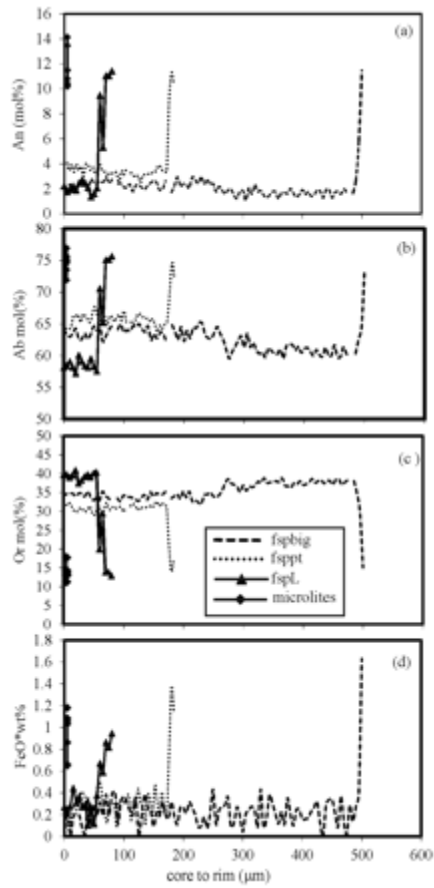
Figure 3. Compositional profiles of anorthoclase phenocrysts (fsppt, fspL, fspbig) and microlites showing the a) An content variation (b); Ab content variation (c) and Or content variation (d) FeO* wt% from the centre of the crystal to the border.
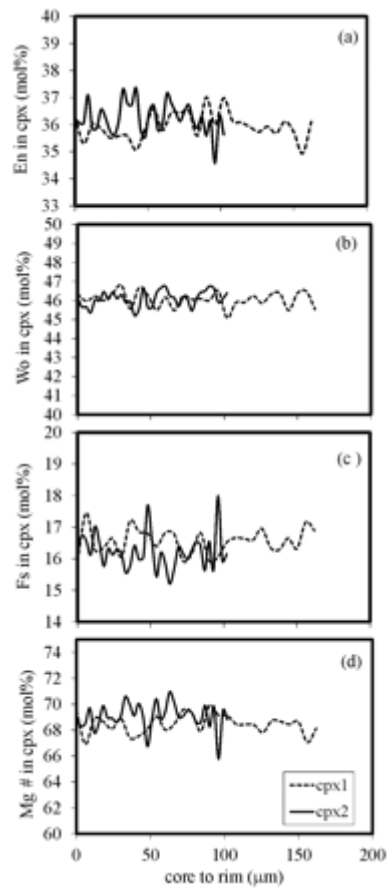
Figure 4. Compositional profiles of diopside phenocrysts (cpx1 and cpx2) showing the En content variation (a), Wo content variation (b), Fs content variation (c) and Mg-number variation (d) from centre of the crystal to border.
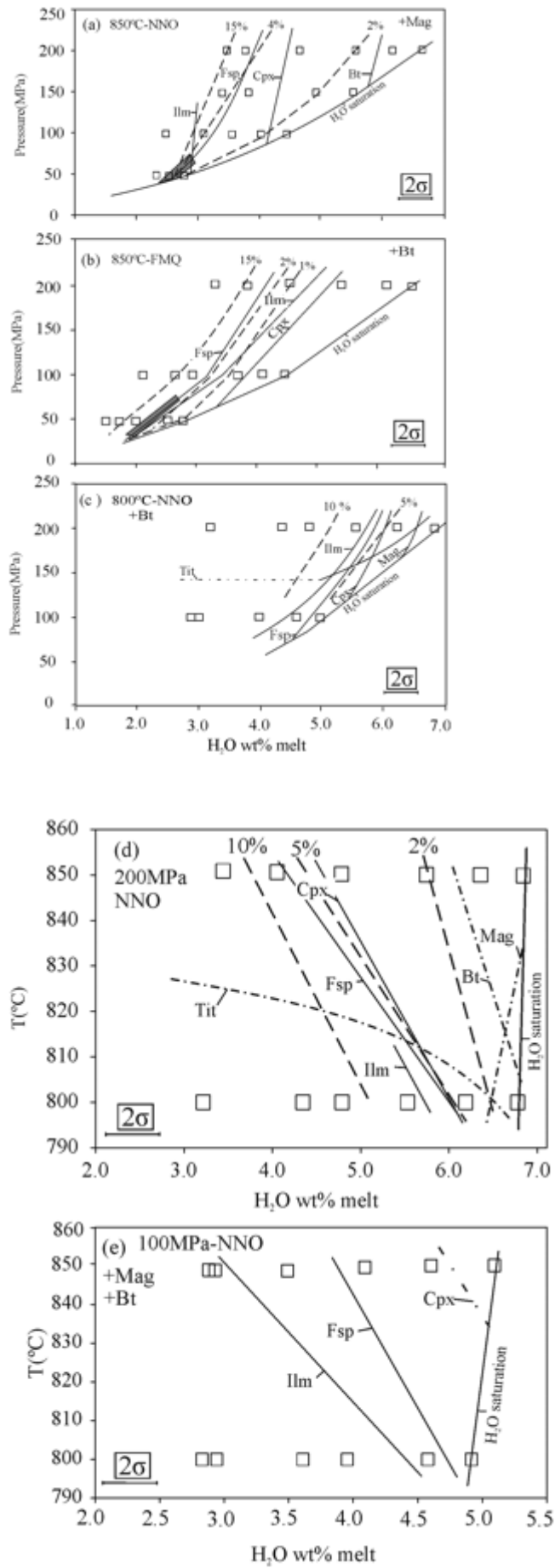
Figure 5. Phase relations of the Montaña Blanca phonolite at a) 850ºC and fO_2~NNO; b) 850ºC and fO_2~FMQ; c) 800ºC and fO_2~NNO for different pressures and water contents in the melt; d) 200 MPa and fO_2~NNO; e) 100 MPa and fO_2~NNO for various temperatures and water contents in the melt. Mag: magnetite, Bt: biotite, Cpx: clinopyroxene, ilm: ilmenite, tit: titanite, fsp: alkali feldspar. Dashed lines are estimated phase boundaries. Numbers above dashed lines indicate crystal content in wt (%). Dashed and dotted lines in plates c, d and e are estimated phase boundaries. Grey band in plate a shows the region where the phenocrysts content and mineral assemblage of the natural obsidian are reproduced.
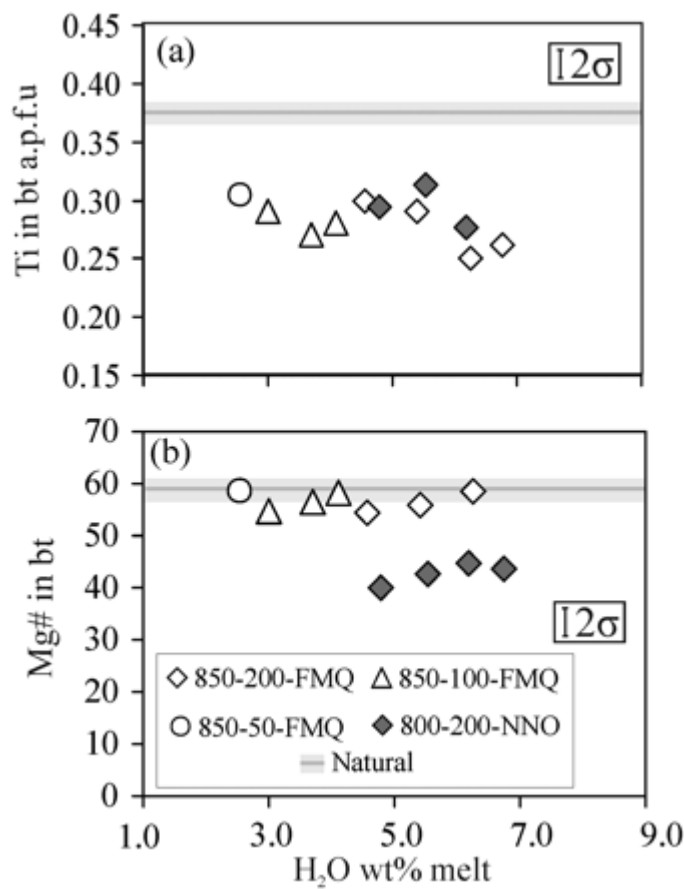
Figure 6. a) Variation of the Ti content in atoms per formula unit (a.p.f.u.) with water content in the melt and b) variation of the Mg-number with water content in the melt Grey horizontal bar shows the natural composition. Numbers next to symbols in the legend indicate temperature, pressure and fO_2 conditions.
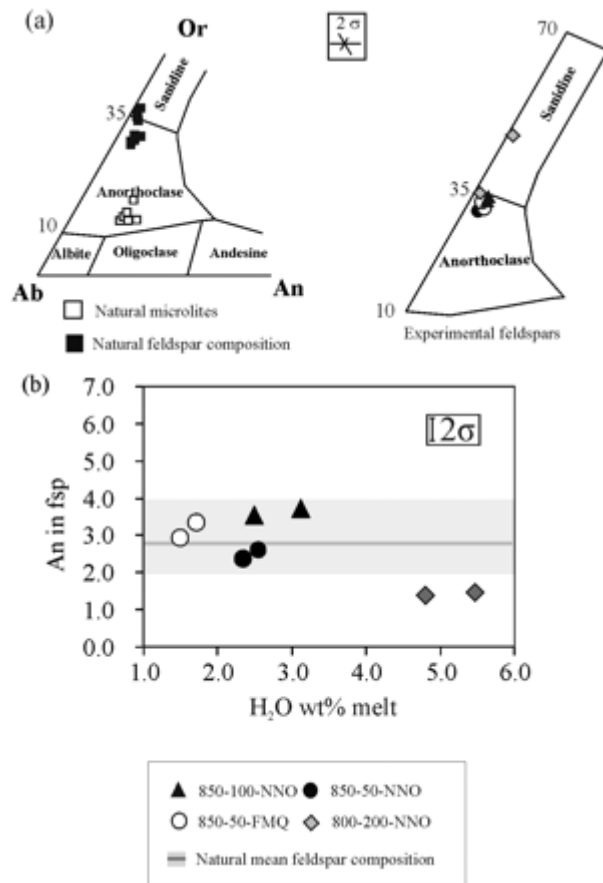
Figure 7. Classification and compositional variation of natural and experimental alkali feldspars. A) Classification of phenocrysts, microlites and experimental alkali feldspars as in Deer et al. (1972). B) variation of the An content in natural and experimental alkali feldspars with water content in the melt. Grey horizontal bar shows the natural composition. Numbers next to symbols in the legend indicate temperature, pressure and fO_2 conditions.
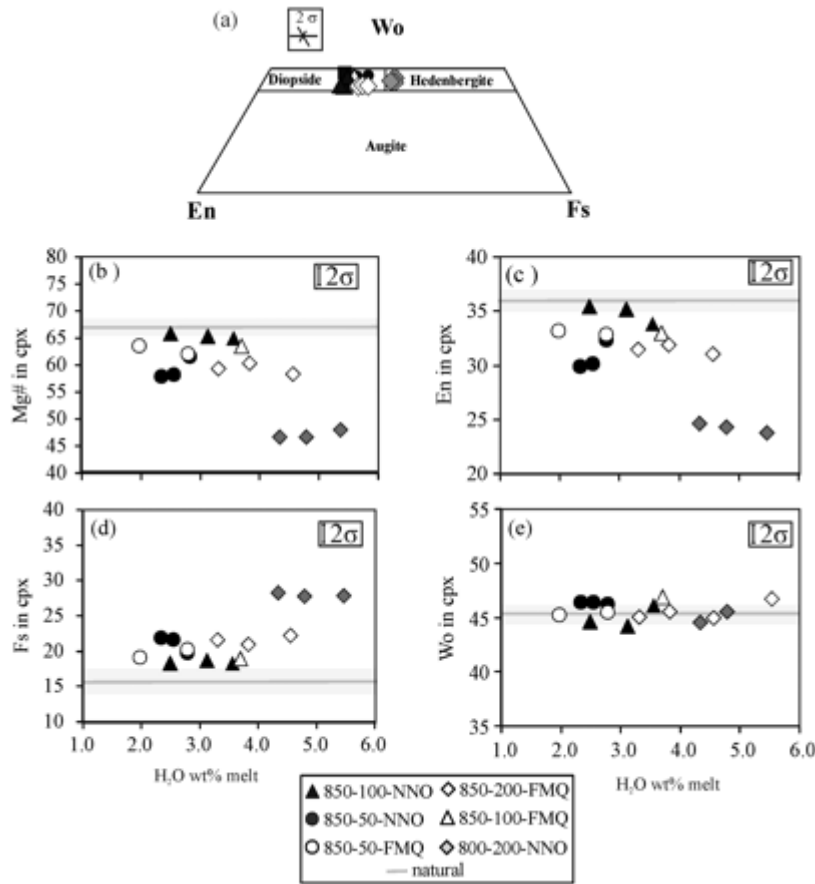
Figure 8. Classification and compositional variation of natural and experimental clinopyroxenes. a) Classification of natural and experimental clinopyroxenes as in Morimoto (1989). b) variation of Mg-number; c) variation of the En content; d) variation of Fs content; e) variation of Wo content in experimental biotites. Grey horizontal bar shows the natural composition. Numbers next to symbols in the legend indicate temperature, pressure and fO$_2$ conditions.

Figure with panels (a) through (j) plotting various oxide compositions against H₂Owt% melt.

Legend:
♦ 850-200-NNO   ◇ 850-200-FMQ
■ 850-150-NNO   △ 850-100-FMQ
▲ 850-100-NNO   ○ 850-50-FMQ
● 850-50-NNO   ◇ 800-200-NNO
━ Natural
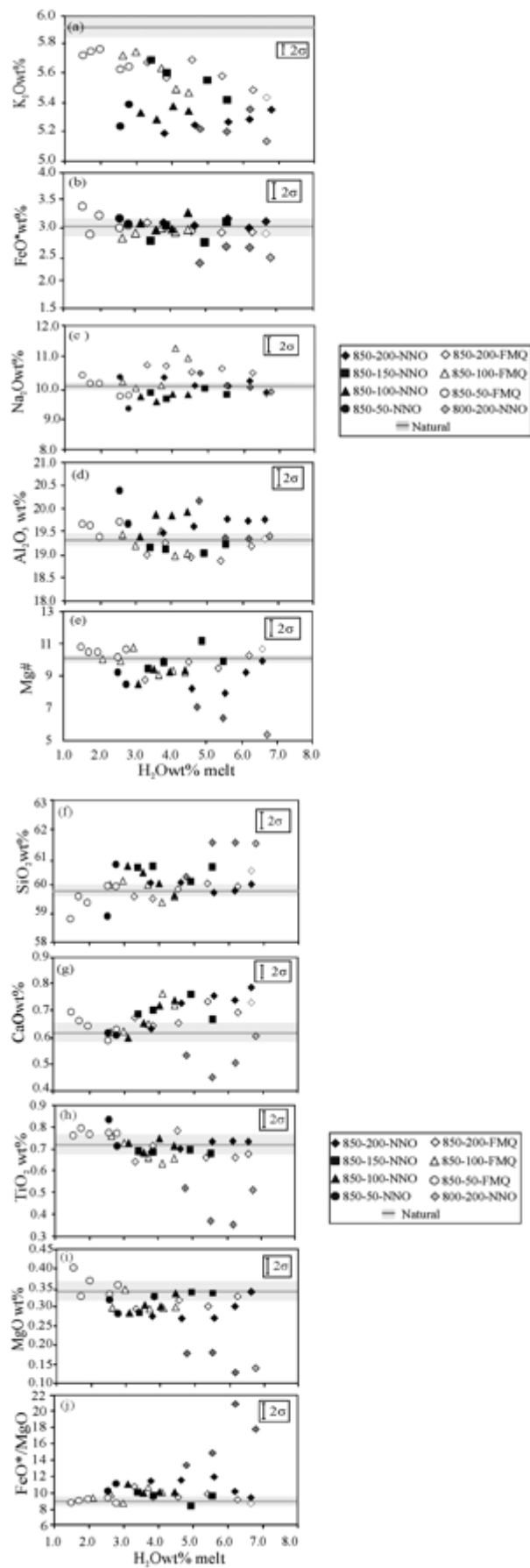
Figure 9. Glass compositional variations of major and minor oxides with water content in the melt (plates a to j). Grey horizontal bar shows the natural composition. Numbers next to symbols in the legend indicate temperature, pressure and fO$_2$ conditions.
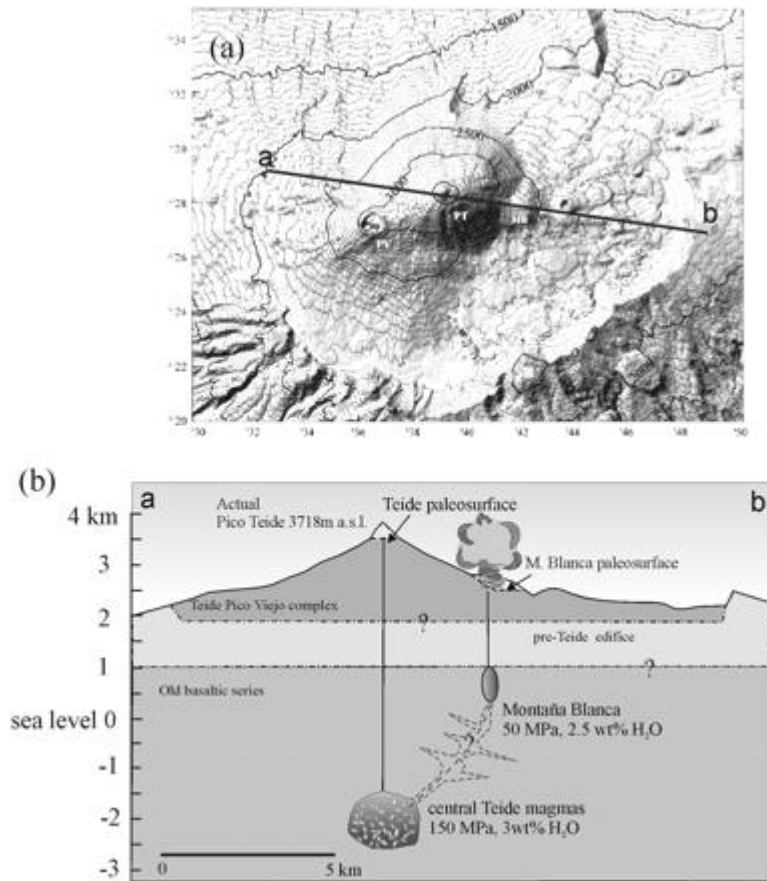
Figure 10. a) Combined shaded relief/contour map of the Las Cañadas caldera showing the Pico Teide (PT), Pico Viejo (PV) and MB (Montaña Blanca; modified from Ablay & Martí, 2000); b) cross section a-b showing the shallow phonolitic plumbing system and the location of the magmatic reservoirs during the UMB eruption (see text). Pre-eruptive conditions for each magma reservoir are from Andújar et al. (2010) for central Teide magmas and this work for Montaña Blanca. Magma reservoir volumes are not at scale.

Table 1:

Major element composition of the natural phonolite: bulk-rock, starting material, glass and mineral phases

	Bulk rock	Starting material	SD	glass	SD	mag	ilm	SD	bt	SD	cpx	SD	anorth mean c	SD	anorth mean r	SD	An-low anorth	SD	An-high anorth	SD	microl	SD
n:		7		15		1	2		2		3		6		6		6		11		6	
SiO$_2$	59·9	59·7	0·3	59·7	0·1	–	0·2	0·1	36·6	0·3	51·6	0·4	66·8	0·6	63·2	1·7	67·7	0·3	64·2	1·1	65·1	0·5
TiO$_2$	0·62	0·64	0·04	0·68	0·07	16·4	50·2	0·5	6·71	0·13	0·59	0·08	0·00	0·0	0·47	0·19	0·09	0·03	0·10	0·03	0·42	0·12
Al$_2$O$_3$	19·3	19·6	0·30	19·3	0·1	1·06	0·05	0·04	12·2	0·3	1·19	0·33	19·2	0·3	20·5	0·2	19·1	0·2	19·4	0·2	20·6	0·2
MgO	0·34	0·33	0·05	0·34	0·04	1·79	2·55	0·08	0·00	0·00	12·18	0·30	0·00	0·0	0·03	0·03	0·01	0·01	0·01	0·01	0·01	0·03
CaO	0·77	0·72	0·02	0·62	0·10	0·09	0·05	0·05	16·4	0·8	21·7	0·5	0·54	0·08	2·42	0·26	0·22	0·03	0·69	0·12	2·41	0·25
MnO	0·20	0·25	0·03	0·18	0·03	2·48	3·17	0·21	0·44	0·08	0·85	0·12	0·00	0·00	0·0	0·0	0·01	0·03	0·02	0·03	0·03	0·06
FeO*	3·5	3·4	0·13	3·0	0·2	73·5	42·6	0·5	12·9	0·1	9·9	0·3	0·1	0·1	1·27	0·38	0·2	0·1	0·3	0·2	0·9	0·25
Na$_2$O	9·84	9·63	0·33	9·93	0·06	0·00	0·02	0·04	0·98	0·09	1·18	0·13	7·04	0·39	8·63	0·27	7·27	0·08	7·43	0·14	8·93	0·33
K$_2$O	5·66	5·74	0·13	5·97	0·09	0·00	0·01	0·02	8·79	0·10	0·07	0·08	5·81	0·14	2·52	0·36	6·67	0·12	5·46	0·18	2·58	0·31
P$_2$O$_5$	0·07			0·17	0·07																	
Total	100			100													101·3	0·6	97·1	0·4	101·0	0·3
Sum	99·9	100·0		97·5	0·6	95·2	98·9	0·8	95·0	1·1	99·2	0·9	99·5	0·8	99·1	0·8						
Mg#				10·1	0·67	4·16			58·4	1·2	67·6	0·9										
Fe$_2$O$_3$c						36·4					6·14	0·94										
FeOc						40·7					4·11	1·16										
a.p.f.u.																						
Fe^{2+}						1·28					0·19	0·03										
Fe^{3+}						1·03					0·12	0·03										
Or													34·3	1·4	14·3	2·1	37·2	0·6	31·5	0·7	14·19	1·79
An													2·70	0·47	11·5	1·0	1·03	0·12	3·33	0·56	11·13	1·23
Ab													63·0	1·5	74·2	1·3	61·7	0·6	65·2	1·0	74·7	1·7
En											35·5	0·5										
Fs											16·1	0·5										
Wo											45·3	0·4										
Phase prop.						0·5	trace		trace		0·65		4·1									

- Bulk-rock composition analysed by inductively coupled plasma mass spectrometry. Starting material, glass, and minerals (mag, magnetite; ilm, ilmenite; bt, biotite; cpx, clinopyroxene; anorth mean, mean composition of alkali feldspar phenocrysts; c, core; r, rim; An-low, An-poor alkali feldspar; An-high, An-rich alkali feldspar; microl, microlites) analysed by electron microprobe. *n*, number of analyses. SD, standard deviation.
  Mg# = 100[Mg/(Mg + Fe*)] in mols for mineral phases;
  Mg# = 100[MgO/(MgO + FeO*)] in wt % for glass and starting material. Or, Ab and An end-members calculated following Deer *et al*. (1972). End-members for clinopyroxene (En, Fs, Wo) calculated following Morimoto (1989). c, calculated by charge balance. Phase prop., phase proportions given in weight % (wt %) and calculated by mass balance. trace, phase abundance <0·1 wt %.
- *Total iron reported as Fe^{2+}.

Table 2:

Experimental conditions and run products

Run	XH$_2$O wt % in.	H$_2$O wt % melt	log fO$_2$ (bar)	ΔNNO	aH$_2$O[e]	Phase assemblage	Σr^2
NNO experiments							
850°C, 200 MPa, 162 h, fH$_2$ (bar) 9·14 [c]			−12·69	0·20			
ae							
MB7	1·00	6·64	−12·85	0·00	0·93	(99·7)Gl + (0·3)Mag	0·5
MB8	0·93	6·17	−12·93	−0·08	0·85	(99·5)Gl + (0·5)Mag	0·6
MB9	0·84	5·58	−13·03	−0·18	0·76	(97·7)Gl + (trace)Mag + (2·3)Bt	0·44
MB10	0·70	4·64	−13·22	−0·37	0·61	(97·8)Gl + (trace)Mag + (2·2)Bt	0·26
MB11	0·57	3·78	−13·43	−0·58	0·48	(82·8)Gl + (0·3)Mag + (2·3)Bt + (trace)Cpx + (14·6)Fsp	0·5
MB12	0·53	3·49				Gl + Mag + Bt + Cpx + Fsp	n.d.
850°C, 150 MPa, 233 h, fH$_2$ (bar) 6·47 [d]							
b							
MB38	0·92	5·54	−12·87	−0·01	0·86	(98·7)Gl + (0·1)Mag + (1·2)Bt	0·3
MB39	0·82	4·92	−12·99	−0·13	0·75	(98·6)Gl + (0·4)Mag + (1·0)Bt	0·21
MB40	0·64	3·85	−13·26	−0·40	0·55	(99·6)Gl + (0·3)Mag + (0·1)Bt + (trace)Cpx	0·48
MB48	0·57	3·41	−13·39	−0·53	0·47	(96·4)Gl + (0·7)Mag + (0·1)Bt + (trace)Cpx + (2·8)Fsp	0·24
850°C, 100 MPa, 195 h, fH$_2$ (bar) 5·6 [d]							
ae							
MB19	1·00	4·45	−13·08	−0·21	0·83	(98·4)Gl + (0·2)Mag + (1·4)Bt	0·68
MB20	0·90	4·02	−13·08	−0·21	0·83	(97·8)Gl + (trace)Mag + (1·9)Bt + (0·32)Cpx	0·35
MB21	0·80	3·56	−13·08	−0·21	0·83	(97·7)Gl + (trace)Mag + (2·1)Bt + (0·20)Cpx	0·52
MB22	0·70	3·12	−13·06	−0·19	0·85	(98·1)Gl + (trace)Mag + (0·9)Bt + (trace)Cpx + (1)Fsp	0·22
MB23	0·56	2·49	−13·18	−0·30	n.d.	Gl + Mag + Bt + Cpx + Fsp + Ilm	n.d.
MB24	0·56	2·49	−13·18	−0·30	n.d.	Gl + Mag + Bt + Cpx + Fsp + Ilm	n.d.
850°C, 50 MPa,389 h, fH$_2$ (bar) 2·42 [c]			−12·71	0·18			
ae							
MB43	1·00	2·79	−	−0·19	0·66	(98·2)Gl + (0·2)Mag + (1·5)Bt + (0·1)Cpx + (trace)Ilm	0·66

Run	$X\text{H}_2\text{O}$ wt % in.	H_2O wt % melt	log $f\text{O}_2$ (bar)	ΔNNO	$a\text{H}_2\text{O}$[e]	Phase assemblage	Σr^2
			13.07				
MB44	0.91	2.55	$\overline{13.12}$	−0.24	0.62	(71.2)Gl + (0.6)Mag + (3.2)Bt + (0.4)Cpx + (24.6)Fsp + (trace)Ilm	0.72
MB45	0.84	2.33	$\overline{13.43}$	−0.36	n.d.	Gl + Mag + Bt + Cpx + Fsp + Ilm	n.d.
800°C, 200 MPa, 114 h, fH₂ (bar) 7.22 [c]			$\overline{13.71}$	0.19			
b							
MB55	1.00	6.77	$\overline{13.61}$	0.25	0.93	Gl + (trace)Bt	
MB56	0.91	6.19	$\overline{13.70}$	0.16	0.85	(96.6)Gl + (3.3)Bt + (trace)Mag + (0.1)Tit	0.06
MB57	0.82	5.53	$\overline{13.81}$	0.06	0.75	(92.1)Gl + (4.4)Bt + (0.2)Mag + (0.5)Tit + (0.8)Cpx + (2.2)Fsp + (trace)Ilm	0.64
MB58	0.71	4.79	$\overline{13.97}$	−0.11	0.62	Gl + Bt + Mag + Tit + Cpx + Fsp + Ilm	n.d.
MB59	0.64	4.35	$\overline{14.10}$	−0.24	n.d.	Gl + Bt + Mag + Tit + Cpx + Fsp + Ilm	n.d.
MB60	0.47	3.18	$\overline{14.37}$	−0.51	n.d.	Gl + Bt + Mag + Tit + Cpx + Fsp + Ilm	n.d.
800°C, 100 MPa, 145 h, fH₂ (bar) 4.92 [d]							
b							
MB67	1.00	4.92	$\overline{13.87}$	0.01	n.d.	Gl + Mag + Bt + Cpx	
MB68	0.93	4.58	$\overline{13.93}$	−0.05	n.d.	Gl + Mag + Bt + Cpx + Fsp	
MB69	0.80	3.95	$\overline{14.06}$	−0.18	n.d.	Gl + Mag + Bt + Cpx + Fsp + Ilm	
MB70	0.73	2.94	$\overline{14.14}$	−0.26	n.d.	Gl + Mag + Bt + Cpx + Fsp + Ilm	
MB71	0.60	2.83	$\overline{14.32}$	−0.43	n.d.	Gl + Mag + Bt + Cpx + Fsp + Ilm	
MB72	0.58	2.83	$\overline{14.35}$	−0.47	n.d.	Gl + Mag + Bt + Cpx + Fsp + Ilm	

FMQ experiments

850°C, 200 MPa, 143 h, fH₂ (bar) 9.744 [d]

Run	$X\text{H}_2\text{O}$ wt % in.	H_2O wt % melt	log $f\text{O}_2$ (bar)	ΔNNO	$a\text{H}_2\text{O}$[e]	Phase assemblage	Σr^2
a							
MB108	1.00	6.64	$\overline{12.90}$	−0.05	0.94	Gl + (trace)Bt	
MB109	0.94	6.26	$\overline{12.94}$	−0.09	0.90	Gl + (trace)Bt	
MB110	0.81	5.40	$\overline{13.08}$	−0.23	0.76	Gl + (trace)Bt	
MB111	0.69	4.56	$\overline{13.26}$	−0.41	0.62	(99.4) Gl + (0.6)Bt + (trace)Cpx + (trace)Ilm	0.72
MB112	0.58	3.83	$\overline{13.47}$	−0.62	0.49	(82.3) Gl + (1.5)Bt + (0.1)Cpx + (trace)Ilm + (16.1)Fsp	0.29
MB113	0.50	3.31	−	−0.77	0.41	(81.4) Gl + (1.4)Bt + (trace)Cpx + (trace)Ilm + (17.2)Fsp	0.26

Run	XH$_2$O wt % in.	H$_2$O wt % melt	log fO$_2$ (bar)	ΔNNO	aH$_2$O[e]	Phase assemblage	Σr^2
			13·62				
*850°C, 100 MPa, 188 h, f*H$_2$ *(bar) 6·66* [d]		a					
MB102	1·00	4·45	−13·25	−0·38	0·87	Gl + (trace)Bt	
MB103	0·92	4·10	−13·32	−0·45	0·80	(99·4)Gl + (0·64)Bt	0·32
MB104	0·83	3·70	−13·48	−0·61	0·67	(98·7)Gl + (1·3)Bt + (trace)Cpx	0·14
MB105	0·67	2·99	−13·73	−0·86	0·51	(97·8)Gl + (0·5)Bt + (0·3)Cpx + (trace)Ilm + (1·4)Fsp	0·24
MB106	0·59	2·62	−13·88	−1·01	0·42	Gl + Bt + Cpx + Ilm + Fsp	
MB107	0·47	2·11	−14·15	−1·28	0·31	Gl + Bt + Cpx + Ilm + Fsp	
*850°C, 50 MPa, 242 h, f*H$_2$ *(bar) 4·7* [d]		a					
MB114	1·00	2·79	−13·69	−0·81	0·64	(98·7)Gl + (0·5)Bt + (0·8)Cpx	0·16
MB115	0·91	2·55	−13·79	−0·91	0·56	(98·4)Gl + (0·6)Bt + (1·0)Cpx	0·20
MB117	0·71	1·98	−14·13	−1·25	0·38	(91·9)Gl + (0·18)Bt + (0·74)Cpx + (trace)Ilm + (6·55)Fsp	0·12
MB118	0·62	1·72	−14·33	−1·45	0·30	(82·6)Gl + (1·9)Bt + (0·63)Cpx + (trace)Ilm + (14·90)Fsp	0·3
MB119	0·54	1·50	−14·56	−1·68	0·23	(76·65)Gl + (1·19)Bt + (0·55)Cpx + (trace)Ilm + (21·61)Fsp	0·17

- XH$_2$O wt % in., initial H$_2$O/(H$_2$O + CO$_2$) in the charge. H$_2$O wt % melt, water content in the melt. log fO$_2$(bar), logarithm of the oxygen fugacity calculated from the experimental fH$_2$. ΔNNO = log fO$_2$ − log fO$_2$ of the NNO buffer calculated at *P* and *T* (Pownceby & O'Neill, 1994). Phase assemblage, numbers in parentheses indicate the phase abundance in the charge in wt %. Gl, glass; Mag, magnetite; Bt, biotite; Cpx, clinopyroxene; Ilm, ilmenite; Fsp, alkali feldspar; Tit, titanite. fH$_2$ (bar) is hydrogen fugacity of the experiment. n.d., not determined.
- [a]Determined by FTIR.
- [b]Determined by the solubility model of Carroll & Blank (1997).
- [c]Determined by using NiPd alloy sensors.
- [d]Calculated using the data obtained from successful NiPd alloys (see text for details).
- [e]aH$_2$O calculated from the solubility model of Carroll & Blank (1997) (see text for details).
- [ae]Extrapolated from capsules run at same *T*, *P* and H$_2$O, and at fO$_2$ ~ FMQ (see text).

Table 3:

FTIR data

Sample	n	Thickness (µm)	SD	5200 (cm^{-1})	SD	4500 (cm^{-1})	SD	Density (g l^{-1})*	SD	H$_2$O (wt %)†	SD
MB108	3	111·3	3·8	0·10	0·00	0·03	0·00	2597·7	1·5	6·64	0·06
MB102	3	145·3	3·1	0·08	0·00	0·03	0·00	2642·7	4·0	4·45	0·16
MB114	3	121·3	11·5	0·04	0·00	0·02	0·00	2678·0	2·0	2·79	0·09

- ↵n, number of spectra. SD, standard deviation. 5200, 4500 (cm^{-1}), absorbance intensity from the 5200 and 4500 peak respectively.
- ↵*Density of the melt calculated as done by Richet *et al.* (2000).
- ↵†Total H$_2$O (wt %) dissolved in the melt calculated as the sum of the water from 5200 and 4500 peaks.

Table 4:

Compositions of experimental biotites (wt %)

	MB55	SD	MB56	SD	MB57	SD	MB58	SD	MB103	MB104	SD	MB105	MB109	SD	MB110	SD	MB111	SD
n:	3		4		4		4		1	2		1	3		3		3	
SiO$_2$	37·3	1·4	37·0	0·6	37·0	1·8	38·7	1·9	39·3	40·8	1·4	40·6	38·1	0·7	36·6	1·3	37·7	1·9
TiO$_2$	4·56	0·31	4·81	0·32	5·35	0·34	5·07	0·63	5·15	5·00	0·29	5·57	4·73	0·21	5·72	0·32	5·97	0·38
Al$_2$O$_3$	12·75	0·54	12·81	0·12	12·19	1·01	12·73	0·51	13·31	13·82	0·48	13·66	13·23	0·28	12·58	0·22	12·80	0·38
FeO*	21·44	1·28	20·92	0·65	20·54	1·24	20·43	1·52	15·06	14·26	1·26	15·86	15·93	0·34	17·37	0·25	17·47	1·24
MnO	0·68	0·03	0·77	0·05	0·66	0·05	0·72	0·07	0·74	0·51	0·14	0·52	0·43	0·11	0·60	0·17	0·62	0·05
MgO	9·41	0·52	9·50	0·30	8·59	0·53	7·65	0·80	11·77	10·38	0·92	10·73	12·68	0·30	12·41	0·13	11·65	0·63
CaO	0·15	0·14	0·00	0·00	0·03	0·02	0·07	0·05	0·38	0·07	0·03	0·03	0·02	0·03	0·03	0·00	0·14	0·21
Na$_2$O	0·76	0·21	0·87	0·17	0·88	0·18	1·21	0·24	1·70	1·93	0·22	1·94	1·32	0·28	1·07	0·27	1·07	0·23
K$_2$O	8·45	0·59	8·55	0·23	8·18	0·54	8·01	0·39	8·52	8·16	0·17	8·20	8·72	0·08	8·77	0·13	8·70	0·51
Sum	95·5	0·8	95·2	1·1	93·4	1·2	94·6	2·2	96·0	95·0	0·6	97·1	95·2	0·7	95·2	0·8	96·1	0·1
Mg#	43·9	0·5	44·7	0·3	42·7	0·4	40·0	0·8	58·2	56·5	0·0	54·7	58·7	0·1	56·0	0·1	54·3	0·5
Ti (a.p.f.u.)	0·26	0·01	0·28	0·02	0·31	0·01	0·29	0·03	0·28	0·27	0·01	0·29	0·25	0·01	0·29	0·02	0·30	0·02

- n, number of analyses. SD, standard deviation. Structural formula calculated according to Dymek (1983): 11 oxygens and OH + F + Cl = 2, and 7 cations − Ti.
- *Total iron reported as FeO.

Table 5:

Compositions of experimental alkali feldspars (wt %)

	MB22	MB24	MB44	SD	MB45	SD	MB57	SD	MB58	SD	MB118	SD	MB119	SD
n:	1	1	2		3		2		2		2		2	
SiO$_2$	64·3	63·8	66·2	0·9	66·1	1·0	66·0	0·1	66·4	0·3	64·7	1·1	64·3	1·4
TiO$_2$	0·31	0·40	0·15	0·09	0·31	0·42	0·07	0·10	0·03	0·04	0·26	0·02	0·25	0·21
Al$_2$O$_3$	19·26	19·31	19·62	0·23	19·35	0·27	18·98	0·13	19·20	0·00	19·26	0·35	18·99	0·08
MgO	0·11	0·19	0·03	0·04	0·01	0·01	0·00	0·00	0·04	0·04	0·14	0·05	0·13	0·10
CaO	0·78	0·62	0·53	0·08	0·48	0·10	0·26	0·00	0·29	0·06	0·68	0·12	0·61	0·05
FeO*	1·51	1·70	0·49	0·27	1·11	1·42	0·51	0·07	0·28	0·07	1·23	0·43	1·25	0·38
Na$_2$O	7·16	5·90	7·30	0·18	7·18	0·15	5·60	0·16	7·24	0·34	7·12	0·32	7·29	0·07
K$_2$O	6·03	5·19	5·59	0·20	5·84	0·29	8·46	0·40	6·30	0·09	5·75	0·05	6·04	0·20
Sum	99·5	97·1	99·9	0·9	100·4	0·8	99·9	0·5	99·8	0·1	99·2	0·6	98·8	0·6
An	3·73	3·55	2·60	0·40	2·36	0·47	1·27	0·01	1·39	0·27	3·33	0·46	2·93	0·30
Ab	61·9	61·1	64·8	0·7	63·6	1·3	49·5	1·9	62·7	1·2	63·1	0·9	62·8	0·3
Or	34·3	35·4	32·6	1·0	34·0	1·7	49·2	1·9	35·9	1·5	33·6	1·3	34·2	0·6

- *n*, number of analyses. SD, standard deviation. An = 100[Ca/(Ca + Na + K)]; Ab = 100[Na/(Ca + Na + K)]; Or = [100K/(Ca + Na + K)]. End-members calculated according to Deer *et al*. (1972).
- *Total iron reported as FeO.

Table 6:

Compositions and end-members of experimental clinopyroxenes (wt %)

	MB 21	SD	MB 22	MB 23	MB 43	SD	MB 44	SD	MB 45	SD	MB 57	MB 58	MB 59	MB 104	MB 111	MB 112	MB 113	MB 114	SD	MB 117	SD
n:	2		1	1	4		6		5		1	1	1	1	1	1	1	1		3	
SiO_2	51·7	0·3	52·3	51·0	51·6	0·8	50·2	0·1	50·5	0·4	50·6	50·0	50·1	50·5	50·3	50·9	50·5	50·9	0·0	49·9	0·8
TiO_2	0·73	0·09	0·86	0·93	1·35	0·48	2·13	0·14	2·06	0·29	0·96	1·11	1·26	1·01	1·38	1·02	1·00	1·27	0·18	1·10	0·16
Al_2O_3	0·37	0·42	0·85	1·25	1·82	0·45	2·45	0·05	2·30	0·29	2·13	2·79	1·96	1·20	2·25	1·31	1·65	1·88	0·21	2·34	1·16
MgO	11·6	0·0	11·9	12·1	10·5	0·5	9·6	0·1	9·5	0·2	7·2	7·1	7·6	11·5	10·1	10·7	10·7	11·0	0·2	11·3	0·6
CaO	22·0	0·2	20·8	21·2	20·8	0·3	20·5	0·2	20·4	0·1	19·9	18·6	19·0	22·8	20·4	21·3	21·3	21·2	0·2	21·4	0·2
MnO	1·08	0·01	1·14	0·96	0·99	0·04	1·03	0·03	1·05	0·10	1·30	1·25	1·34	0·75	1·04	0·94	1·11	0·95	0·41	1·46	0·41
FeO^{*}	11·2	0·0	11·3	11·2	11·4	0·2	12·3	0·1	12·3	0·2	14·9	14·5	15·4	11·8	12·9	12·5	13·1	12·0	0·1	11·6	0·5
Na_2O	1·30	0·28	0·92	1·28	1·54	0·31	1·68	0·10	1·79	0·06	1·72	2·04	2·14	0·43	1·66	1·27	0·71	0·74	0·06	0·86	0·38
K_2O	0·00	0·00	0·00	0·00	0·10	0·04	0·00	0·02	0·10	0·02	0·30	0·44	0·25	0·00	0·00	0·00	0·00	0·00	0·00	0·00	0·00
Sum	100·0	0·0	100·0	100·0	100·0	0·4	100·0	0·3	100·0	0·2	99·1	97·7	99·1	100·0	100·0	100·0	100·0	100·0		100·0	
wt % glass	11·5	–	16·2	16·1	–		–		–		–	–	–	13·1	7	4	18	20·2		17·5	
FeOc	6·35	1·43	10·03	6·18	9·24	0·48	9·42	0·34	9·52	1·00	12·9	12·5	11·30	8·81	8·43	8·58	10·54	10·9	0·16	7·62	2·71
Fe_2O_3c	5·37	1·55	1·39	5·58	2·39	0·63	3·18	0·61	3·11	1·26	2·45	2·51	4·76	3·29	4·96	4·41	2·81	1·24	0·26	4·42	3·39
a.p.f.u.																					
Fe^{2+}c	0·20	0·05	0·32	0·19	0·29	0·02	0·30	0·01	0·30	0·03	0·41	0·40	0·36	0·28	0·27	0·27	0·34	0·35	0·00	0·24	0·09
Fe^{3+}c	0·15	0·04	0·04	0·16	0·07	0·02	0·09	0·02	0·09	0·04	0·07	0·07	0·14	0·09	0·14	0·13	0·08	0·04	0·01	0·13	0·10
En	33·8	0·1	35·2	35·4	32·3	0·9	30·2	1·6	29·9	0·4	23·6	24·3	24·7	33·0	31·1	31·9	31·5	32·8	0·9	33·2	1·2
Fs	18·3	0·1	18·7	18·4	19·8	0·7	21·6	1·4	21·8	0·3	27·3	27·7	28·3	18·9	22·2	21·0	21·6	20·2	0·0	19·1	0·6
Wo	46·1	0·2	44·2	44·6	46·2	0·3	46·4	0·5	46·4	0·4	46·7	45·6	44·6	46·9	44·9	45·5	45·1	45·4	0·3	45·2	1·0
Mg#	64·9	0·0	65·3	65·8	62·1	1·5	58·2	2·9	57·8	0·6	46·3	46·7	46·6	63·6	58·3	60·4	59·3	61·9	0·7	63·5	0·5

- wt % glass, weight per cent of glass subtracted from the original electron microprobe analysis (see text for details). *n*, number of analyses. SD, standard deviation. c, calculated by charge balance. a.p.f.u., atoms per formula unit. En, Fs, Wo calculated according to Morimoto (1989). Mg# = $100[Mg/(Mg + Fe^{*})]$.
- *Total iron reported as Fe^{2+}.

Table 7:

Composition of experimental glasses (wt %) normalized to 100% anhydrous basis

	n	SiO_2	TiO_2	Al_2O_3	MgO	CaO	MnO	FeO^*	Na_2O	K_2O	Sum	Original sum	Peralkalinity	$Na_2O + K_2O$	Mg#	FeO^*/MgO
NNO experiments																
MB7	4	60·04	0·68	19·8	0·34	0·79	0·23	3·13	9·9	5·14	100·0	93·0	1·1	15·0	9·8	9·3
SD		0·57	0·05	0·4	0·02	0·04	0·03	0·19	0·2	0·08		0·3			0·8	0·9
MB8	5	59·79	0·68	19·7	0·30	0·74	0·19	3·01	10·3	5·29	100·0	93·6	1·1	15·6	9·1	10·0
SD		0·18	0·04	0·3	0·03	0·05	0·03	0·25	0·2	0·17		0·6			0·5	0·5
MB9	4	59·72	0·6	19·8	0·27	0·76	0·24	3·18	10·1	5·27	100·0	94·3	1·1	15·4	7·8	11·8
SD		0·38	0·03	0·3	0·02	0·02	0·03	0·10	0·1	0·05		0·3			0·5	0·9
MB10	5	60·10	0·64	19·6	0·27	0·73	0·22	3·06	10·1	5·25	100·0	96·4	1·1	15·4	8·1	11·5
SD		0·68	0·05	0·5	0·03	0·03	0·04	0·12	0·2	0·07		0·9			0·9	1·5
MB11	3	60·08	0·63	19·5	0·28	0·64	0·23	3·11	10·4	5·19	100·0	96·9	1·2	15·6	8·1	11·3
SD		0·84	0·06	0·6	0·01	0·06	0·02	0·10	0·2	0·04		0·3			0·5	0·8
MB19	6	59·64	0·66	19·9	0·34	0·74	0·22	3·30	9·8	5·35	100·0	94·4	1·1	15·2	9·2	9·9
SD		0·56	0·02	0·4	0·04	0·06	0·05	0·11	0·2	0·12		1·5			0·8	0·9
MB20	5	60·06	0·69	19·9	0·30	0·73	0·17	2·99	9·8	5·38	100·0	95·7	1·1	15·2	9·2	10·0
SD		0·45	0·04	0·6	0·02	0·02	0·05	0·18	0·2	0·07		0·5			0·6	0·7
MB21	5	60·46	0·63	19·9	0·30	0·66	0·21	2·97	9·6	5·29	100·0	97·3	1·1	14·9	9·3	9·8
SD		0·70	0·03	0·8	0·02	0·03	0·06	0·14	0·1	0·13		0·4			0·7	0·7
MB22	4	60·70	0·67	19·4	0·28	0·60	0·16	3·10	9·8	5·34	100·0	97·7	1·1	15·1	8·4	10·9
SD		0·91	0·06	0·5	0·03	0·04	0·05	0·26	0·1	0·04		0·6			0·3	0·4
MB38	7	60·65	0·62	19·2	0·33	0·67	0·13	3·12	9·8	5·43	100·0	94·4	1·1	15·2	9·8	9·5
SD		0·18	0·09	0·1	0·04	0·08	0·10	0·22	0·3	0·08		0·5			1·5	1·5
MB39	6	60·13	0·64	19·0	0·34	0·77	0·82	2·74	10·0	5·51	100·0	95·9	1·2	15·5	11·0	8·2
SD		0·94	0·07	0·4	0·04	0·07	1·46	0·24	0·3	0·15		1·5			1·4	1·1
MB40	6	60·68	0·63	19·1	0·33	0·71	0·19	3·06	9·7	5·61	100·0	94·6	1·2	15·3	9·7	9·5
SD		0·21	0·05	0·2	0·05	0·06	0·04	0·13	0·2	0·14		0·9			1·6	1·7
MB43	4	60·74	0·66	19·7	0·28	0·61	0·19	3·09	9·4	5·40	100·0	97·6	1·1	14·8	8·4	11·0
SD		0·60	0·02	0·6	0·02	0·03	0·02	0·11	0·2	0·05		0·3			0·6	0·9
MB44	2	58·9	0·62	20·4	0·32	0·78	0·22	3·18	10·4	5·24	100·0	99·1	1·1	15·6	9·1	10·1
SD		0·6	0·02	0·1	0·0	0·10	0·04	0·04	0·38	0·07		0·4			1·1	1·3
MB48	6	60·6	0·63	19·2	0·28	0·69	0·24	2·77	9·89	5·70	100·0	96·4	1·2	15·6	9·3	9·9
SD		0·9	0·13	0·2	0·06	0·09	0·12	0·50	0·32	0·10		0·9			1·4	1·6
MB55	4	61·5	0·46	19·4	0·14	0·61	0·14	2·46	9·91	5·36	100·0	92·4	1·1	15·3	5·3	15·3
SD		0·4	0·07	0·1	0·06	0·03	0·07	0·26	0·31	0·18		1·2			1·3	1·1
MB56	5	61·6	0·30	19·3	0·13	0·51	0·11	2·65	10·1	5·36	100·0	93·7	1·2	15·5	4·6	20·9
SD		0·2	0·03	0·1	0·05	0·07	0·12	0·20	0·18	0·18		0·5			0·7	1·8
MB57	4	61·5	0·31	19·4	0·18	0·45	0·15	2·67	10·1	5·21	100·0	92·2	1·2	15·3	6·3	14·8
SD		0·3	0·04	0·1	0·04	0·03	0·11	0·06	0·46	0·04		1·2			1·4	2·4
MB58	4	60·3	0·47	20·2	0·18	0·54	0·25	2·36	10·5	5·23	100·0	91·4	1·1	15·7	6·9	13·7
SD		0·3	0·08	0·2	0·04	0·07	0·17	0·15	0·43	0·20		1·0			1·0	2·4
FMQ experiments																
MB102	3	59·6	0·6	19·0	0·30	0·73	0·19	2·98	11·0	5·52	100·0	94·5	1·3	16·5	9·1	10·0
SD		0·4	0·1	0·0	0·00	0·07	0·04	0·20	0·2	0·1		0·1			0·6	0·7
MB103	4	59·4	0·6	19·0	0·30	0·77	0·15	2·93	11·3	5·5	100·0	96·0	1·3	16·8	9·2	9·9
SD		0·3	0·0	0·2	0·02	0·08	0·07	0·14	0·2	0·0		0·2			0·6	0·7
MB104	4	60·0	0·6	19·5	0·29	0·65	0·13	3·01	10·1	5·6	100·0	93·8	1·2	15·7	8·9	10·5
SD		0·2	0·1	0·2	0·05	0·06	0·04	0·19	0·4	0·1		0·7			1·8	2·4
MB105	3	60·2	0·7	19·2	0·34	0·63	0·29	2·92	10·0	5·8	100·0	93·9	1·2	15·8	10·6	8·6
SD		0·3	0·0	0·1	0·04	0·03	0·09	0·21	0·1	0·1		0·4			1·4	1·3
MB106	3	60·0	0·7	19·4	0·30	0·62	0·13	2·82	10·2	5·7	100·0	96·9	1·2	15·9	9·8	9·7
SD		0·3	0·1	0·4	0·04	0·03	0·06	0·48	0·1	0·0		0·5			2·6	2·8
MB107	5	58·9	0·8	19·4	0·37	0·76	0·20	3·37	10·7	5·5	100·0	95·0	1·2	16·2	9·9	9·2

51

	n	SiO₂	TiO₂	Al₂O₃	MgO	CaO	MnO	FeO*	Na₂O	K₂O	Sum	Original sum	Peralkalinity	Na₂O + K₂O	Mg#	FeO*/ MgO
SD		0·3	0·0	0·1	0·04	0·05	0·05	0·10	0·1	0·2		0·8			1·1	1·3
MB108	3	60·5	0·6	19·3	0·34	0·74	0·15	2·91	9·8	5·4	100·0	93·7	1·1	15·2	10·5	8·5
SD		0·4	0·1	0·2	0·02	0·10	0·06	0·15	0·2	0·1		0·1			0·5	0·4
MB109	5	60·0	0·6	19·2	0·33	0·70	0·19	2·93	10·5	5·5	100·0	94·4	1·2	16·0	10·1	9·0
SD		0·4	0·1	0·1	0·02	0·04	0·06	0·26	0·2	0·1		0·5			1·3	1·3
MB110	3	60·1	0·6	18·9	0·30	0·74	0·17	2·93	10·7	5·6	100·0	94·8	1·3	16·3	9·3	9·7
SD		0·4	0·0	0·0	0·01	0·02	0·11	0·19	0·4	0·2		0·9			0·5	0·5
MB111	3	59·9	0·7	19·0	0·32	0·66	0·21	2·96	10·6	5·7	100·0	95·0	1·2	16·3	9·7	9·3
SD		0·4	0·1	0·3	0·02	0·04	0·15	0·29	0·3	0·1		0·4			0·7	0·7
MB112	3	59·5	0·7	19·3	0·33	0·65	0·18	3·02	10·8	5·6	100·0	97·1	1·2	16·3	9·8	9·3
SD		0·2	0·0	0·1	0·02	0·02	0·06	0·29	0·3	0·0		0·4			1·0	1·1
MB113	3	59·6	0·6	19·0	0·29	0·68	0·22	3·11	10·8	5·7	100·0	96·6	1·3	16·4	8·6	10·6
SD		0·3	0·1	0·2	0·03	0·10	0·06	0·12	0·3	0·1		0·2			0·6	0·8
MB114	5	60·0	0·7	19·7	0·36	0·63	0·16	3·05	9·8	5·7	100·0	94·8	1·1	15·5	10·5	8·6
SD		0·2	0·0	0·2	0·02	0·03	0·09	0·08	0·2	0·1		0·7			0·6	0·5
MB115	4	60·0	0·7	19·7	0·33	0·59	0·25	3·01	9·8	5·6	100·0	94·8	1·1	15·4	10·0	9·2
SD		0·3	0·1	0·2	0·05	0·05	0·09	0·25	0·1	0.		1·0			1·7	1·8
MB117	2	59·4	0·7	19·4	0·37	0·65	0·31	3·24	10·2	5·8	100·0	94·9	1·2	16·0	10·3	9·1
SD		0·0	0·0	0·0	0·08	0·06	0·08	0·31	0·2	0·2		0·8			2·8	2·8
MB118	4	59·6	0·7	19·6	0·33	0·67	0·21	2·89	10·2	5·8	100·0	95·2	1·2	16·0	10·3	8·9
SD		0·6	0·1	0·3	0·04	0·06	0·10	0·46	0·3	0·1		1·5			1·5	1·5
MB119	3	58·8	0·7	19·7	0·40	0·70	0·16	3·41	10·5	5·7	100·0	97·0	1·2	16·2	10·6	8·6
SD		0·5	0·1	0·4	0·05	0·08	0·14	0·29	0·0	0·2		1·1			1·9	1·8

- All analyses are normalized to 100% anhydrous. Original totals before alkali correction are reported. SD, standard deviation. *n*, number of analyses. Peralkalinity = (Na + K)/Al in mols. Mg# = 100(MgO/(MgO + FeO*)) in wt %; FeO*/MgO is a wt % ratio.
- *Total iron reported as Fe^{2+}.